High-Temporal Resolution Polarimetric X-Band Doppler Radar Observations of the 20 May 2013 Moore, Oklahoma, Tornado

JAMES M. KURDZO

School of Meteorology, and Advanced Radar Research Center, University of Oklahoma, Norman, Oklahoma

DAVID J. BODINE

Advanced Study Program, National Center for Atmospheric Research, Boulder, Colorado

BOON LENG CHEONG

Advanced Radar Research Center, University of Oklahoma, Norman, Oklahoma

ROBERT D. PALMER

School of Meteorology, and Advanced Radar Research Center, University of Oklahoma, Norman, Oklahoma

(Manuscript received 24 October 2014, in final form 9 March 2015)

ABSTRACT

On 20 May 2013, the cities of Newcastle, Oklahoma City, and Moore, Oklahoma, were impacted by a long-track violent tornado that was rated as an EF5 on the enhanced Fujita scale by the National Weather Service. Despite a relatively sustained long track, damage surveys revealed a number of small-scale damage indicators that hinted at storm-scale processes that occurred over short time periods. The University of Oklahoma (OU) Advanced Radar Research Center's PX-1000 transportable, polarimetric, X-band weather radar was operating in a single-elevation PPI scanning strategy at the OU Westheimer airport throughout the duration of the tornado, collecting high spatial and temporal resolution polarimetric data every 20 s at ranges as close as 10 km and heights below 500 m AGL. This dataset contains the only known polarimetric radar observations of the Moore tornado at such high temporal resolution, providing the opportunity to analyze and study finescale phenomena occurring on rapid time scales. Analysis is presented of a series of debris ejections and rear-flank gust front surges that both preceded and followed a loop of the tornado as it weakened over the Moore Medical Center before rapidly accelerating and restrengthening to the east. The gust front structure, debris characteristics, and differential reflectivity arc breakdown are explored as evidence for a "failed occlusion" hypothesis. Observations are supported by rigorous hand analysis of critical storm attributes, including tornado track relative to the damage survey, sudden track shifts, and a directional debris ejection analysis. A conceptual description and illustration of the suspected failed occlusion process is provided, and its implications are discussed.

1. Introduction

The 20 May 2013 EF5 tornado that affected the cities of Newcastle, Oklahoma City, and Moore, Oklahoma, was observed by numerous radar systems in and around the metropolitan area of Oklahoma City with varying update rates, spatial resolutions, distances/angles to the storm, and capabilities (e.g., polarimetric moments). The University of Oklahoma Advanced Radar Research Center's PX-1000 transportable, polarimetric, X-band radar combined temporal resolution of 20 s and spatial resolution of 112 m in range (oversampled to 30 m) with high-quality polarimetric estimates and a serendipitously close range to form a distinct perspective regarding finescale phenomena in the storm.

The Moore storm is particularly suited for this type of analysis because of its strength, location, and high-profile nature. These factors combined to result in the most detailed storm survey in National Weather Service (NWS) history, consisting of more than 4200 damage

Corresponding author address: James M. Kurdzo, Advanced Radar Research Center, 3190 Monitor Ave., Norman, OK 73019.
E-mail: kurdzo@ou.edu

DOI: 10.1175/MWR-D-14-00357.1

© 2015 American Meteorological Society

indicators (Atkins et al. 2014a; Burgess et al. 2014). Of particular interest in the damage survey results was the path of the tornado in the vicinity of the Moore Medical Center (MMC), where a distinct shift in direction and a loop were observed. During analysis of PX-1000 data, a number of finescale shifts in the track of the tornado were discovered that were not readily apparent in the damage survey. This study analyzes these track shifts, forward speed changes, debris ejections, and polarimetric tornadic debris signatures (TDSs; Ryzhkov et al. 2002, 2005) in order to differentiate/compare each of the observed shift instances with the observed loop at the MMC. Such shifts in track are not easily observable without extremely rapid update rates commonly associated with tornado-scale research radars.

Cyclic supercells (Darkow and Roos 1970; Fujita et al. 1970) have been of key interest to many tornado-related research thrusts due to the relation between their rarity and impact. Cyclic mesocyclogenesis, specifically, was first conceptualized by Burgess et al. (1982), while a later detailed case study by Beck et al. (2006) added to the conceptual theory behind mesocyclone occlusions and new mesocyclogenesis. Finer-scale studies regarding cyclic tornadogenesis through the use of higher temporal and spatial resolutions have also been carried out, and it has been shown that cyclic supercells can be prolific tornado producers and are often the type of supercell associated with tornado outbreaks (Dowell and Bluestein 2002a,b; Tanamachi et al. 2012). These studies have also shown it is not uncommon for brief, weak tornadoes to precede longer-lived, stronger tornadoes.

Furthermore, recent high-resolution mobile radar observations of tornadoes during convective field experiments have provided numerous other areas of insight into supercell and tornado dynamics (e.g., Bluestein et al. 2004; Wurman and Alexander 2005; Bluestein et al. 2007b; Kosiba and Wurman 2010; Wurman et al. 2012; Kosiba and Wurman 2013; Wurman and Kosiba 2013), as well as storm-scale microphysics and thermodynamics (e.g., Markowski et al. 2002, 2012; Kosiba et al. 2013; Marquis et al. 2012). Specifically, polarimetric observations have driven entirely new studies of mesoscale and storm-scale phenomena, particularly studies of storm microphysics. TDSs, for example, have provided remote tornado detection capabilities (Ryzhkov et al. 2005; Bluestein et al. 2007a; Kumjian and Ryzhkov 2008; Palmer et al. 2011; Snyder and Ryzhkov 2014) and the potential for new conceptual formulation exists such as the use of TDS observations for tornado strength and debris type determination (Schultz et al. 2012; Bodine et al. 2013, 2014). Ryzhkov et al. (2005) defined the TDS as an area of high reflectivity, low differential reflectivity (Z_{DR}), and low copolar cross-correlation coefficient (ρ_{HV}) collocated with a tornadic vortex signature in radial velocity (v_r). Kumjian and Ryzhkov (2008) identified high Z_{DR} values along the inflow side of the forward-flank precipitation echo, which they termed the Z_{DR} arc. Later studies have shown that the Z_{DR} arc results from size sorting (Kumjian and Ryzhkov 2009; Dawson et al. 2014), and in cyclic supercell cases, formation and dissipation of the Z_{DR} arc is associated with mesocyclogenesis (Kumjian et al. 2010).

A number of important questions remain unanswered regarding our understanding of the relationship between mesocyclogenesis/tornado genesis, dissipation, and cyclic evolution. While this is due in large part to the wide range of possible scenarios in severe local storms and their environments, an added caveat is the lack of extremely rapid update rates combined with high-quality data (Heinselman et al. 2008; Heinselman and Torres 2011). When the combination of a cyclic storm with rapid radar updates and high data quality is available, the potential for new conceptual formulations exists. Recently, a series of mobile radar platforms (e.g., Wurman and Randall 2001; Biggerstaff et al. 2005; Weiss 2009; Bluestein et al. 2010; Isom et al. 2013; Pazmany et al. 2013) have provided new insight into the dynamic and cyclic nature of mesocyclogenesis (Ziegler et al. 2001; Beck et al. 2006; French et al. 2008) and tornado structures and life cycles (Wurman et al. 2010; French et al. 2013; Wurman and Kosiba 2013; Houser et al. 2015; Snyder and Bluestein 2014).

Rear-flank downdrafts (RFDs), specifically, have been a focus of numerous supercell and tornado studies [summarized in Markowski (2002)]. While in situ thermodynamic/kinematic observations and studies of RFDs have become quite common since VORTEX and VORTEX2 (e.g., Markowski et al. 2002; Grzych et al. 2007; Finley and Lee 2008; Hirth et al. 2008; Lee et al. 2012; Markowski et al. 2012; Atkins et al. 2014b; Skinner et al. 2014), rapid-scanning polarimetric datasets of complex RFD evolutions are scarce in the literature. Additionally, the relationship between cyclic mesocyclogenesis, cyclic tornadogenesis, and ongoing RFD/rear-flank gust front surges (RFGFS) can vary considerably from storm to storm.

The comparison between RFGFSs and mesocyclone structure has been a common research theme in recent years (Adlerman et al. 1999; Finley and Lee 2004; Adlerman and Droegemeier 2005; Skinner et al. 2014), as has the comparison between RFGFSs and ongoing tornadic debris (Houser 2013). The Moore storm displayed numerous instances of RFGFSs and subsequent debris ejections; however, these surges occurred on extremely rapid time scales and did not result in tornadogenesis or tornadic dissipation, nor did they result in a new mesocyclone in the conventional sense. Adlerman

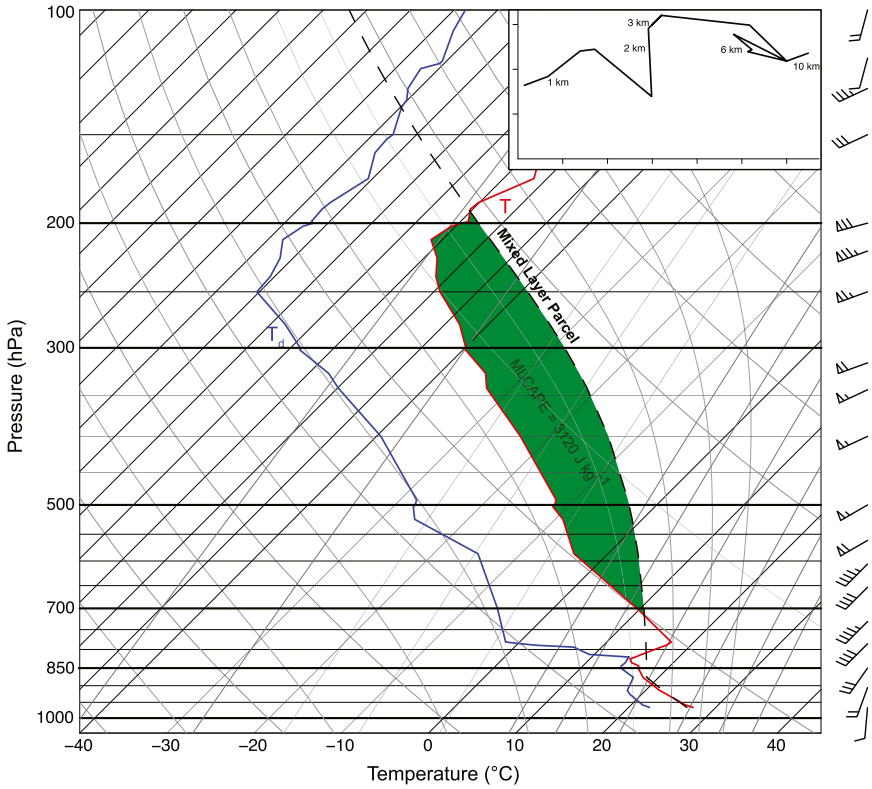

FIG. 1. Sounding released by NWS Norman at 1800 UTC 20 May 2013. Thermodynamic sounding consists of temperature T (°C; red), dewpoint temperature T_d (°C; blue), mixed-layer parcel path (dashed black), and unstable region shaded in green. Top-right inset shows the hodograph, with winds plotted in m s^{-1} (axis tick marks are in 5 m s^{-1} steps), and critical heights labeled along the hodograph. On the right side of the figure, flags, wind barbs, and half wind barbs denote 50, 10, and 5 kt (1 kt = 0.5144 m s^{-1}), respectively.

et al. (1999) described the conventional (or "classic") occlusion process as the development of an evaporatively driven RFD wrapping cyclonically around the mesocyclone, causing a gust front surge and updraft development at midlevels. As the new, two-celled structure of updrafts progresses, the upshear updraft weakens as it is cut off from storm-relative inflow. The single instance of near occlusion in the Moore storm, herein called a "failed" occlusion, is of particular interest among the RFGFSs. Section 2 of this paper discusses the general event overview, and section 3 presents the system, data, and processing methods. Sections 4 and 5 present a detailed overview of the PX-1000 dataset and a discussion of its implications, respectively, while section 6 offers a summary and the conclusions.

2. Event overview and tornado track

During the early afternoon hours of 20 May 2013, a 500-hPa trough extended from southeastern South Dakota through western Nebraska and Kansas and into northeastern New Mexico, while the right entrance region of a 31 m s^{-1} midlevel jet streak and 15 m s^{-1} of 850-hPa flow out of the south-southwest were situated over central Oklahoma. A sharp dryline was located in a north-northeast/south-southwest orientation west of the Interstate 35 (I-35) corridor in central Oklahoma, and the 1800 UTC KOUN sounding in Norman indicated mixed-layer (ML) CAPE of 3120 J kg^{-1}, mixed-layer convective inhibition (MLCIN) of 33 J kg^{-1}, a mixed-layer lifting condensation level (MLLCL) of 890 m, 0–6-km AGL bulk shear of 27 m s^{-1}, and 0–1-km storm relative helicity of 131 m^2 s^{-2} (Fig. 1). A stationary surface boundary was coexistent with the dryline, which by 1800 UTC, had begun to bulge into central Oklahoma with surface winds directly to the east turning out of the south-southeast.

The first radar returns of the Moore storm appeared at approximately 1900 UTC, west of Bridge Creek (via PX-1000, the KTLX WSR-88D, and the TOKC TDWR; not shown). By 1934 UTC, three distinct cells and associated mesocyclones were evident, with one near Mustang, a second east of Tuttle, and a third just north of Bridge Creek. By 1946 UTC, the northern cells had dissipated,

and the southern cell had rapidly strengthened and organized, with a defined hook structure in reflectivity factor at horizontal polarization (Z_{HH}) and a $\sim$60 m s^{-1} inbound/outbound radial velocity differential (Δv_r) across the mesocyclone (which was $\sim$2 km in horizontal diameter at the sampled elevation). Between 1946 and 1956 UTC, a surge of precipitation occurred around the southern edge of the hook, with tornadogenesis estimated at 1956 UTC according to the NWS damage survey (Burgess et al. 2014) and gate-to-gate PX-1000 Δv_r of $\sim$35 m s^{-1}. A low-Z_{HH} region in the hook and a polarimetric debris signature quickly became evident in low-level radar scans.

The tornado rapidly strengthened, producing EF3–EF4 damage within 4 min of tornadogenesis. A series of Z_{HH} and v_r examples from key times during the tornado are shown in Fig. 2, as well as a hand analysis of the PX-1000-indicated tornado track (using the location of maximum Δv_r) and the contoured maximum EF-scale damage ratings from Burgess et al. (2014). The track is interpolated using a periodic interpolating cubic spline curve (Lee 1989), which is necessary because of the wide native beamwidth of PX-1000 (1.8°; see the following section). A photograph of the tornado is shown in Fig. 3, taken at approximately 2018 UTC (just after impacting Briarwood Elementary School).

While EF3 damage was apparent throughout the majority of the tornado's lifetime, EF4 damage did not occur again until approximately 2010 UTC, although this may be attributable to the sparse density of structures in northern Newcastle. From 2014 to 2023 UTC, a constant swath of EF4 damage, with occasional EF5 damage, was evident in the damage survey. As seen in the PX-1000 data, the tornado shifted east and north multiple times before turning sharply to the north and looping just west of the MMC at I-35 between 2023 and 2024 UTC. After this loop, Δv_r decreased and forward ground speed increased, but consistent EF3 (and common EF4) damage continued through approximately 2030 UTC, with dissipation occurring around 2035 UTC. The NWS survey indicated that the tornado lasted 39 min and had a pathlength of 23 km and a maximum damage width of 1.7 km. Of the 4531 damaged structures, over 3500 were residential buildings (Atkins et al. 2014a), and more than 300 structures experienced EF4/EF5 damage (Burgess et al. 2014).

3. PX-1000 system description, data collection, and processing

The PX-1000 radar is a transportable, polarimetric, X-band, dish-based platform mounted on a trailer that can be moved as necessary for various field campaign requirements (Table 1; Cheong et al. 2013a). Operating at 100-W peak power on each channel (for simultaneous independent H/V transmit/receive), the pulse compression scheme described in Kurdzo et al. (2014) is used in order to achieve the necessary sensitivity for meteorological data collection. The resulting sensitivity is approximately 14 dBZ at 50-km range, and the native range resolution is 112 m. The 1.8-m-diameter parabolic dish results in a 1.8° azimuthal resolution at 9.55 GHz, and the scanning technique used on 20 May resulted in an effective beamwidth of 2.0° [utilizing the effective beamwidth formulation in Doviak and Zrnić (1993)]. The range gates and azimuths are oversampled to 30 m and 1.0°, respectively.

Because of the use of pulse compression, a blind range during transmission of the long pulse (67 μs) exists, meaning no returns can be measured within 10.3 km of the radar. To mitigate this issue, the time-frequency multiplexing (TFM) method described in Cheong et al. (2013a) is utilized to fill the blind range with a short pulse (2 μs). The resulting sensitivity is lower in the 10.3 km surrounding the radar, however, strong echoes such as those associated with the tornado/parent supercell are sufficiently resolved and do not hinder the analysis presented in this study. This discrepancy is more apparent in weaker echoes, as seen in Fig. 4 where a circular area of lower sensitivity is apparent. The Moore tornado skirted the edge of the blind range, but for the majority of its lifetime was just beyond this range.

Additionally, in order to achieve high-quality estimates, the multilag method detailed in Lei et al. (2012) is used for moment estimation. The multilag method is especially valuable for ρ_{HV} estimation in low signal-to-noise (SNR) situations. This method, when combined with the TFM technique, allows for ρ_{HV} estimates that are less susceptible to low SNRs, resulting in significantly increased accuracy and smooth transitions across the blind range (Cheong et al. 2013b). In areas of high spectrum width, however, the multilag Gaussian fit does not hold. Therefore, gates with lag-2 spectrum widths greater than 5 m s^{-1} as well as SNR greater than 10 dB were processed with standard pulse-pair moment estimates.

PX-1000 is capable of custom scanning strategies, ranging from volumetric scans to PPI scans and RHI scans. Before the onset of severe weather on 20 May, PX-1000 was set to run at a constant 2.6° elevation (PPI) scan at a rotation rate of 18° s^{-1}, resulting in an update rate of 20 s. Although other scanning strategies would have been useful for various types of analysis (e.g., volumetric analysis), the 20-s update rate, even at a single elevation, resulted in a polarimetric dataset capable of detecting rapidly evolving areas of the storm that a volumetric scanning strategy would have missed.

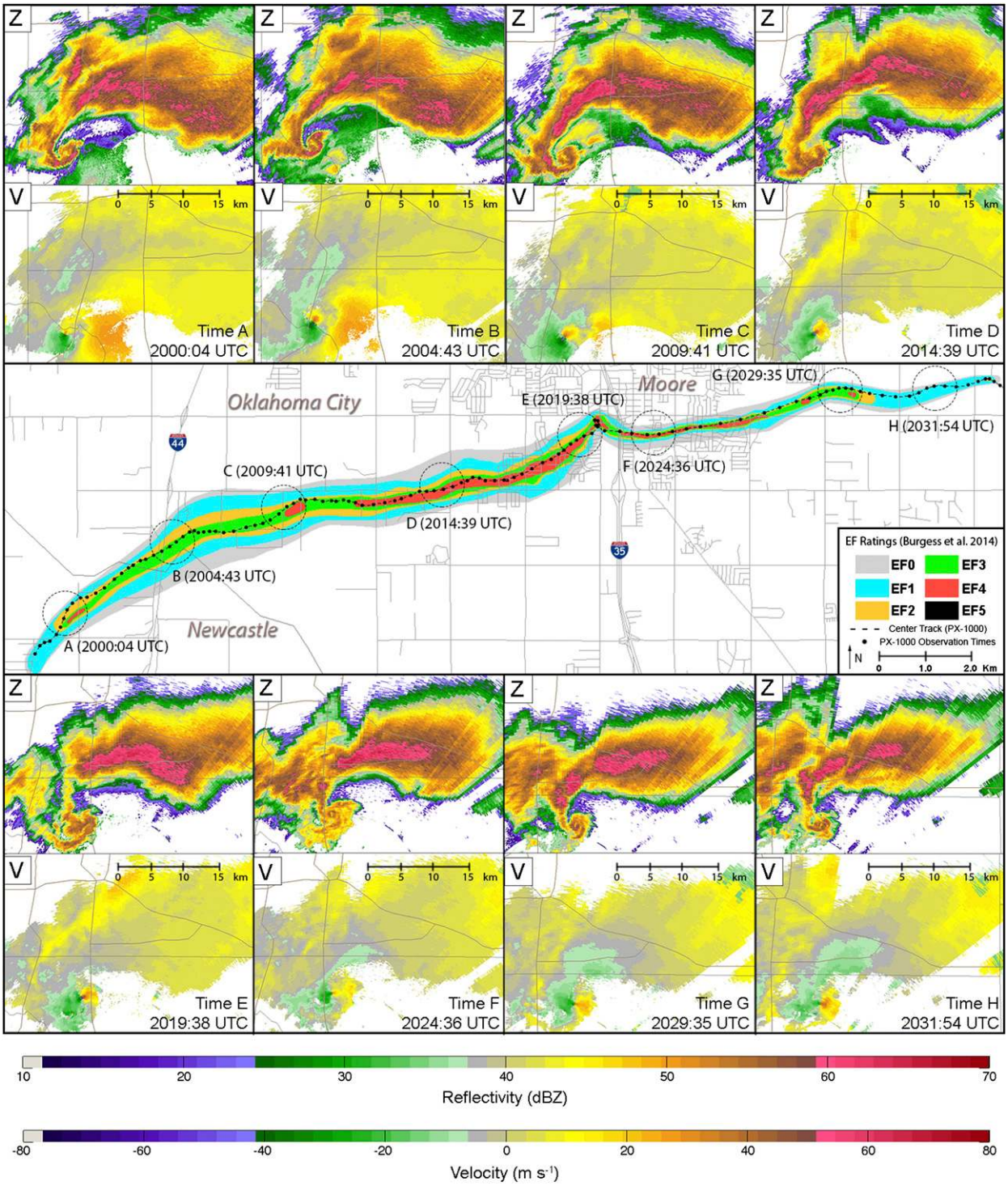

FIG. 2. EF-scale damage ratings [colored shading, from Burgess et al. (2014)], vortex center track from PX-1000 Δv_r data (dotted black line), PX-1000 observation times (black dots), and sample Z_{HH} and v_r data from different times/locations along the tornado track shown in top/bottom frames (denoted by circles and times A–H).

FIG. 3. The tornado in Moore, OK, at approximately 2018 UTC. View is from just east of Indian Hills Rd. and 48th Ave. NW, looking to the NNW. (Photograph courtesy Gabriel Garfield, NOAA/NWS.)

PX-1000 I/Q data were processed with a TFM matched filter to generate moment data. A total of 100 pulses were used for moment estimates. Velocity dealiasing was completed manually using standard unfolding techniques. With availability of high-quality polarimetric estimates, attenuation correction was applied to the data using differential attenuation parameterizations (Bringi et al. 1990; Jameson 1992; Park et al. 2005). The values suggested by Snyder et al. (2010) at the X band were used for correction of Z_{HH} and Z_{DR}. The dual-Doppler example shown in section 4 was completed using a 14 km × 14 km grid with spacing of 300 m in both dimensions, centered on the tornado. A Barnes's analysis (Barnes 1964) with smoothing lengths of 100 m in both dimensions and three passes (Majcen et al. 2008) was used along with a two-dimensional variant of the dual-Doppler method described in Shapiro and Mewes (1999):

$$u = \frac{[(y - y_1)R_2 v_{r2} - (y - y_2)R_1 v_{r1}]}{[(x - x_2)(y - y_1) - (x - x_1)(y - y_2)]}, \quad (1)$$

$$v = \frac{[(x - x_2)R_1 v_{r1} - (x - x_1)R_2 v_{r2}]}{[(x - x_2)(y - y_1) - (x - x_1)(y - y_2)]}, \quad (2)$$

where x and y are meridional and zonal positions, respectively, to an analysis point with respect to a radar, R is the range to the analysis point from a radar, and v_r is the radial velocity measured by a radar. The subscripts 1 and 2 refer to radar 1 (PX-1000) and radar 2 (KTLX), respectively.

Finally, the maximum radial velocity increase (v_i) calculations were formulated using a sliding window along each radial of the single-Doppler v_r field from PX-1000. To compare with the values seen in Lee et al. (2012) at a fair resolution difference, the window size was set to approximately 1 km, or 34 range gates. The maximum absolute value of radial velocity differential was determined for each gate based on this sliding window.

4. PX-1000 radar observations

a. Early tornado track

Shortly before tornadogenesis, and after the dissipation of the northern two cells, a fourth cell with a weakly rotating updraft rapidly approached the main supercell from the south. This southern cell began to merge with the main supercell at nearly the exact time of tornadogenesis (~1956 UTC; Fig. 2a) and was not fully ingested into the main supercell until approximately 2012 UTC (Fig. 2c). While the lack of three-dimensional dual-Doppler data prevents the ability to analyze this cell merger in depth (and data assimilation is beyond the scope of this paper), various studies regarding cell mergers via both simulations and observations have suggested a potential role in tornadogenesis (Bluestein

TABLE 1. System characteristics and 20 May operational settings for PX-1000.

System characteristics		20 May operational settings	
Transmitter type	Dual solid state power amplifiers (SSPAs)	Nyquist velocity	15.7 m s^{-1}
Operating frequency	9550 MHz	Unambiguous range*	65 km
PRF	1–2000 Hz	PRF	2000 Hz
Radiating center	2.5 m AGL	Polarimetric processing	Multilag
Sensitivity	<20 dBZ at 50 km	Sensitivity	14 dBZ at 50 km
Observable range	60 km	Scanning strategy	PPI
Antenna gain	38.5 dBi	Elevation angle	2.6°
Antenna diameter	1.8 m	Rotation rate	18° s^{-1}
3-dB beamwidth	1.8°	Update rate	20 s
Polarization	Dual linear, simultaneous H/V (SHV)	Long pulse length	67 μs
Polarimetric isolation	26 dB	Short pulse length	2 μs
Max rotation rate	50° s^{-1}	Range resolution	112 m
Peak power	100 W	Range oversampling	30 m
Pulse width	1–69 μs	Effective beamwidth	2.0°
Chirp bandwidth	5 MHz	Azimuthal oversampling	1.0°
Max duty cycle	20%	Long pulse bandwidth	2.2 MHz, nonlinear frequency modulation (NLFM)
Min gate spacing	30 m	Short pulse bandwidth	0.5 MHz at −3 dB

* A result of the use of a fill pulse.

and Weisman 2000; Lee et al. 2006; Wurman et al. 2007; Hastings et al. 2014).

Before and during the cell merger, the mesocyclone displayed distinctly different RFGF characteristics compared with the latter part of the storm's life, highlighted by the lack of RFGFSs (to be discussed in depth in upcoming sections). By completion of the merger with the southern cell, a distinct tornadic vortex signature (Brown et al. 1978), quasi-circular TDS (Ryzhkov et al. 2002, 2005), and Z_{DR} arc (Kumjian and Ryzhkov 2008) were all apparent, along with classic supercellular Z_{HH} and v_r structures (Fig. 4; Lemon and Doswell 1979). Additionally, a possible low-reflectivity ribbon (LRR; Snyder et al. 2013) is apparent in some of the early Z_{HH} data.

Figure 5 provides a time series of maximum EF-scale damage rating (interpreted in time from the NWS damage survey), maximum Δv_r, forward ground speed of the tornado, the direction of vortex movement, and an event timeline highlighting numerous key events. The middle three plots are smoothed using a five-point sliding window on account of the wide native PX-1000 beamwidth. The timeline depicts start times of RFGFSs and temporary track shifts, the loop at MMC, the existence of a Z_{DR} arc breakdown, and a southern surge of precipitation discussed in later subsections.

A gradual increase in maximum Δv_r to values greater than 100 m s^{-1} (and occasionally over 120 m s^{-1}) was apparent, coinciding with a large swath of EF4 and EF5 damage indicators seen in the NWS damage survey (Burgess et al. 2014). During the early stages of the tornado, forward ground speed was maintained between 8 and 11 m s^{-1}, with occasionally slower movements during apparent "track shifts." These track shifts are marked on the timeline and can also be seen in the directional time series plot, where the vortex center occasionally turned slightly to the right temporarily before recovering to the same general northeasterly motion. These track shifts can be seen in the middle panel of Fig. 2. The second of these shifts, occurring around 2008–2010 UTC, was associated with a slowed forward ground speed (~4 m s^{-1} slower than previously), as well as an area of EF4 damage indicators.

b. RFGF surges and debris ejections

Throughout the lifetime of the Moore tornado, a series of track shifts and debris ejections were observed in the PX-1000 data. Debris ejections in this context are defined as an area of debris ejected from the core tornado vortex along a line typically to the south of the tornado and have been referred to as debris "tails" or debris deformation events in previous studies (Houser 2013; Houser et al. 2015). For the purposes of this study, debris ejections/tails are differentiated from the TDS by an asymmetry in the TDS with a nondebris separation between the TDS and the tail necessary for identification. A conceptual diagram of debris ejections/tails is provided in Fig. 6, and a series of examples from the Moore case, discussed further in the following sections, can be seen in Fig. 7.

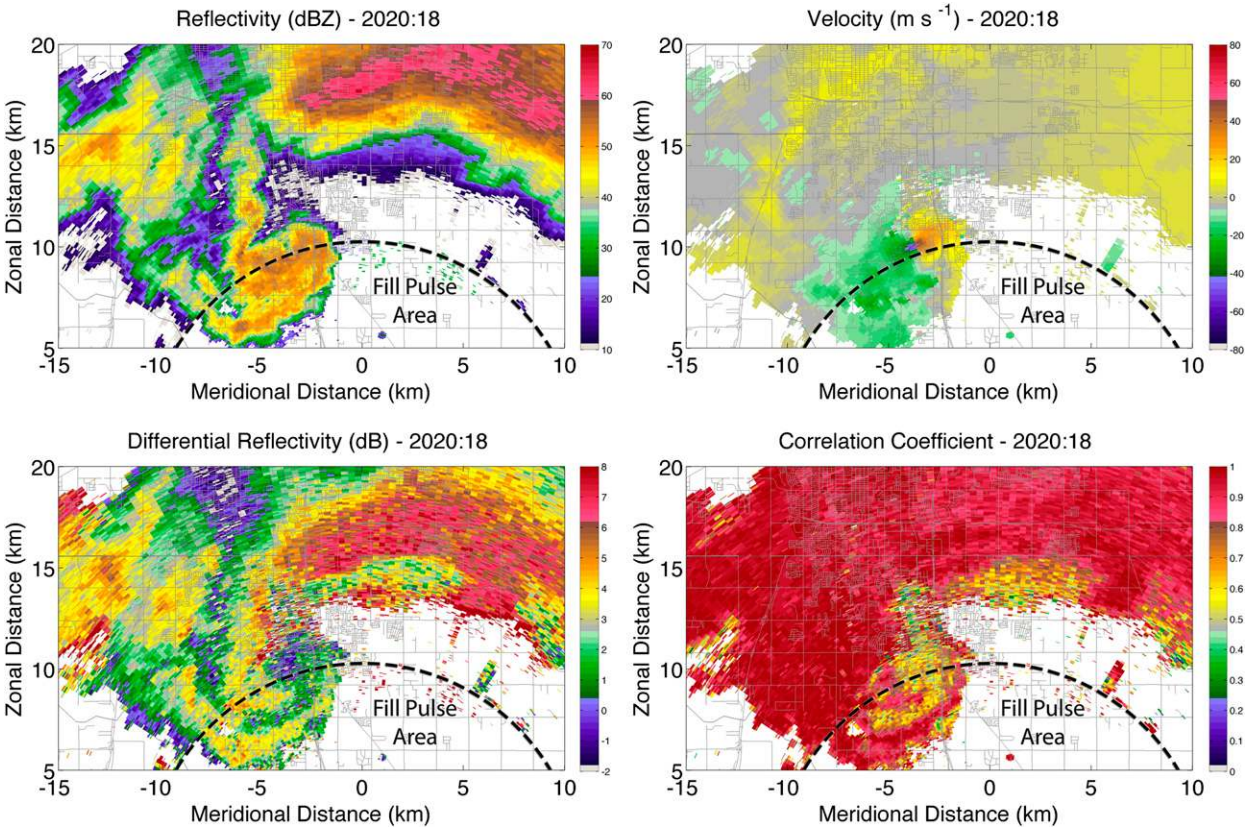

FIG. 4. (from top left, clockwise) PX-1000 Z_{HH}, dealiased v_r, ρ_{HV}, and Z_{DR} at 2020:18 UTC. The dashed semicircle represents the northern half of the PX-1000 fill pulse edge, approximately 10.3 km from the radar. Distances labeled are from the radar location, which is to the south of the frame.

As with debris in a TDS, polarimetric radar can be used to identify debris in one of these ejections/tails via relatively low values in ρ_{HV} and Z_{DR}, and relatively high values in Z_{HH}. Bodine et al. (2013) suggest that debris at the S band can be differentiated using Z_{HH} values greater than 42.5 dBZ collocated with ρ_{HV} values below 0.825. These thresholds have been applied to the PX-1000 data at the X band in order to locate debris inside and outside the tornadic circulation with the expectation that the values will yield viable results at the X band. Since the only debris thresholding studies have taken place at the S band, the scattering differences between the S and X band are poorly understood, so it is assumed that S-band values perform reasonably well at the X band. For the purposes of this study, S-band values should be close enough for proper discrimination of debris from meteorological scatterers, which typically have considerably higher ρ_{HV} (Dolan and Rutledge 2009; Snyder et al. 2010).

Furthermore, it is contended that debris tails have a direct association with RFGFSs, since a surge of high winds would be likely to carry debris from the tornadic circulation, especially in strong tornadoes in populated areas that contain a significant amount of debris (Fig. 6). Additionally, an RFGFS implies an intensification of the downdraft, which would likely enhance debris fallout into the RFD. While the analysis of RFGFSs with high-temporal and high-spatial resolution dual-Doppler observations would be ideal, the lack of radar datasets in the Oklahoma City metropolitan area on 20 May with the temporal resolution of PX-1000 makes this type of analysis in the Moore tornado impossible, especially due to the fact that many of the debris ejections observed existed on time scales less than 1–2 min. Therefore, for the Moore case, it is argued that the PX-1000 observations of debris ejections can be used as a proxy to analyze RFGFSs at high temporal resolution. To support this assumption, an overlay of single-Doppler maximum radial velocity increase (v_i) contours at 13 m s^{-1} with a ρ_{HV} underlay for each of the first six debris ejections is shown in Fig. 7. Only the first six debris ejections are chosen for this analysis since the final two ejections were primarily in the cross-beam direction, leading to a sub-optimal radar viewing angle. The first two cases also

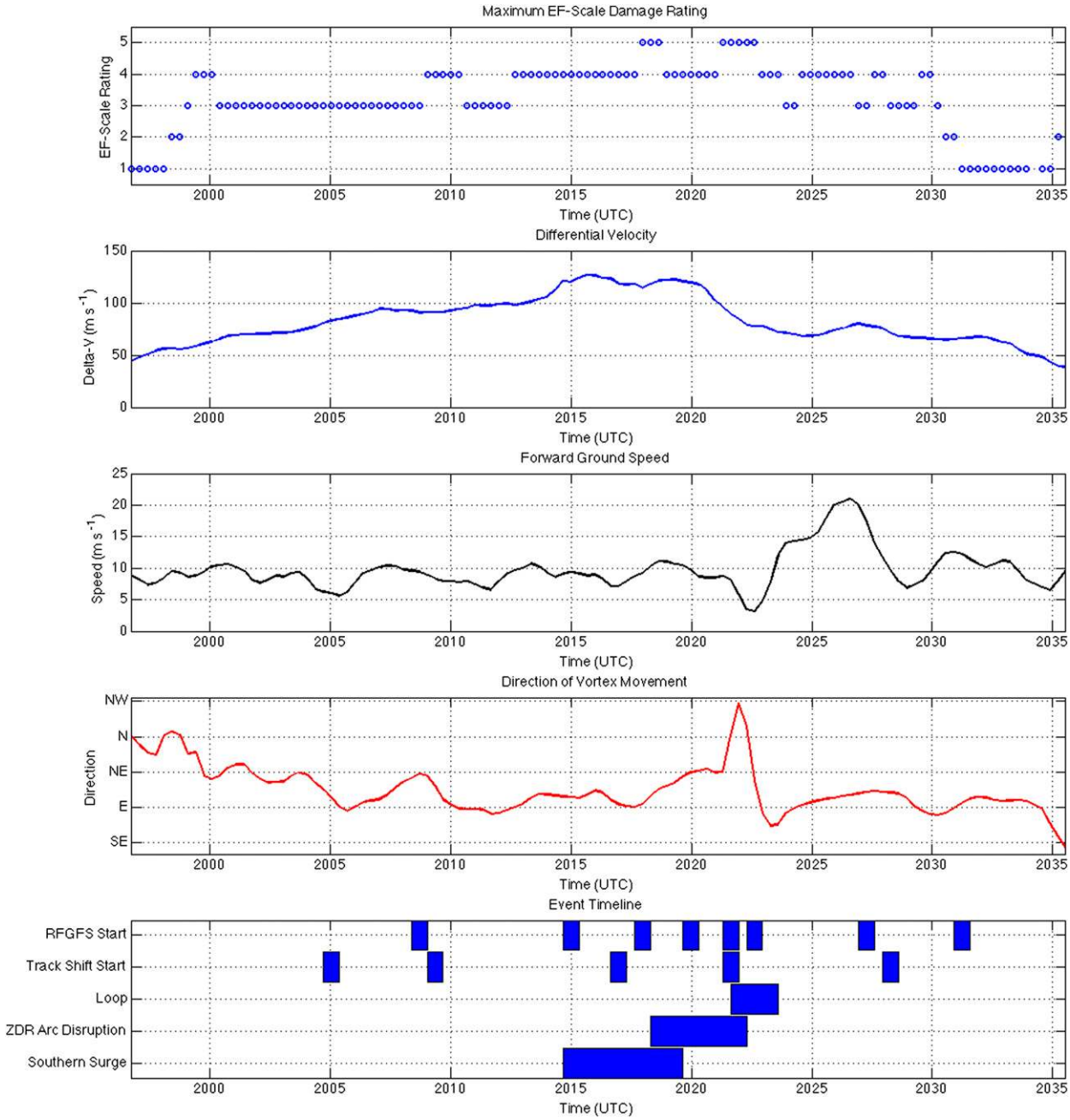

FIG. 5. (top four panels, from top to bottom) Instantaneous maximum EF-scale ratings interpreted from Burgess et al. (2014), time series of maximum Δv_r (m s^{-1}), vortex forward ground speed (m s^{-1}), and direction of vortex movement. (bottom) Timeline of various observed characteristics of the tornado/supercell, including (from top to bottom) RFGFSs, track shifts, the loop at the MMC, the existence of a Z_{DR} arc disruption, and a strong southern surge of hydrometeors just before the beginning of the occlusion process.

consisted of significant cross-beam components, making their appearance much less obvious in Fig. 7. The 13 m s^{-1} threshold was chosen based on observations from Lee et al. (2012) in RFGFSs.

It can be argued, as shown in Fig. 7, that each of the debris ejections was associated with a v_i maximum in either a collocated or slightly lagged sense, suggesting that near-surface convergent flow along RFGFSs caused debris lofting and, therefore, a manifestation of each RFGFS in the ρ_{HV} field. In some of the cases, especially the first three RFGFSs, a distinct area of convergence directly behind the debris ejection is not apparent;

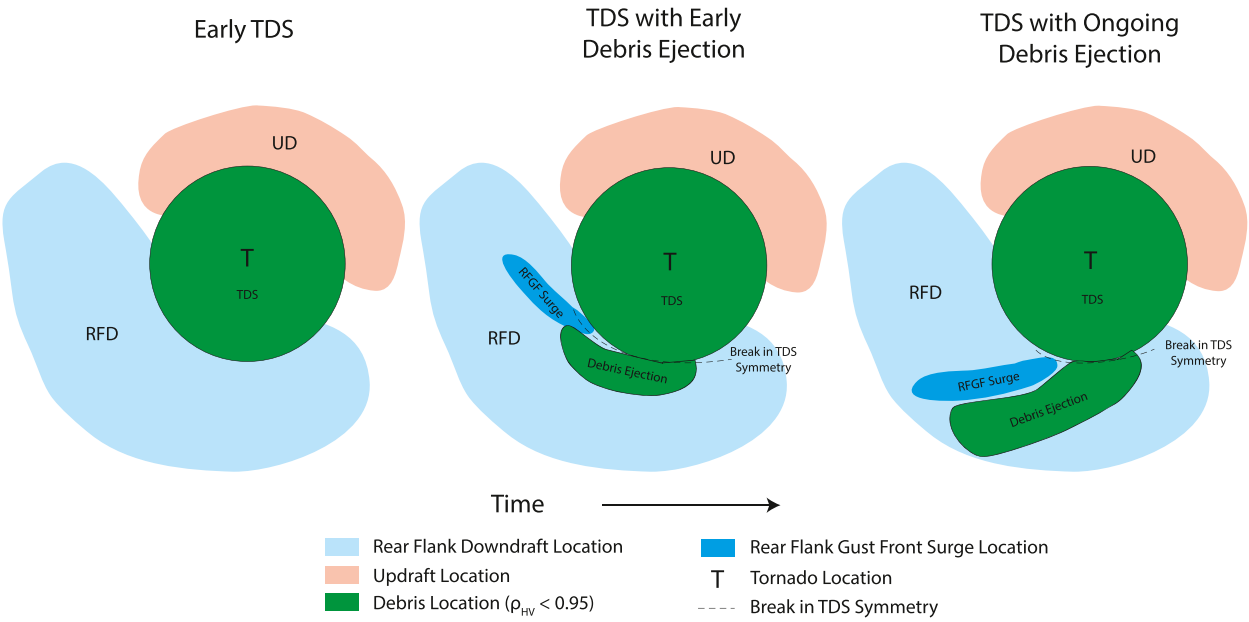

FIG. 6. Conceptual diagram of the debris ejection process. (left) The early stages of the tornado displaying a typical ρ_{HV} minimum within the TDS. (middle) As the tornado matures, the RFD develops a concentrated area of high low-level winds marking an RFGFS and a debris ejection. The debris ejection/RFGFS is qualitatively defined as a debris "tail" that protrudes beyond the usually symmetric TDS. (right) Later in the debris ejection process, the concentrated RFGFS moves around the TDS, pushing debris farther from the TDS, characterized by an extended tail of low ρ_{HV}.

however, a nonsymmetry in the convergence field to the south of the TDS is apparent near the observed debris. Although dual-Doppler observations are not available for the majority of RFGFS cases during the Moore tornado, a suitable baseline between PX-1000 and the KTLX WSR-88D was available for three scans, one of which was during a debris ejection. A dual-Doppler analysis with KTLX was performed at 2022:17 UTC, shown in Fig. 8. Convergence values higher than $0.1\,s^{-1}$ are contoured in dashed lines. Along the southern debris ejection, pockets of high convergence coexist with the lowest areas of ρ_{HV}. Given the observation height of roughly 470 m, debris is likely being lofted by updrafts along the RFGFS, as implied by low level convergence and the continuity equation.

Assuming this is true for all observed debris ejections throughout the lifetime of the Moore tornado, a series of RFGFSs can be analyzed using the high-resolution PX-1000 polarimetric data. The debris ejections (referred to uniformly as RFGFSs from this point forward) occurred regularly along the track of the tornado and often preceded track shifts (Fig. 9). The eight RFGFSs, labeled R1–R8, are detailed in Table 2, and their beginning stages are labeled in the event timeline in Fig. 5. With the lack of high-temporal resolution dual-Doppler observations, the existence of debris in "tail" shapes can be used to analyze characteristics of the RFGFSs. By manually tracing the RFGFS signatures and thresholding for Z_{HH} and ρ_{HV} values consistent with debris, radar gates associated with RFGFS debris can be compared in direction from the tornado location in a moving reference frame. These locations are shown in polar coordinate histograms in Fig. 10. Each gate (i.e., oversampled volume size; roughly $30 \times 117 \times 117\,m^3$ in dimension at a range of 10.5 km) is counted as one value for a direction in each plot; however, each plot is normalized in the radial dimension (the number of total gates) to allow the plot to be used primarily for directivity.

It is important to note that this method serves only to indicate gates that contain debris; the debris density is not known. Additionally, it is likely that the amount of debris available for fallout is proportional to tornado intensity and size relative to available damage indicators, meaning that the debris ejections likely contain more debris as the tornado moved through central Moore; therefore, the exact magnitude of each plot in the radial dimension should not be used as a proxy for strength. Instead, the speed values in Table 2 are likely more appropriate. The speed values in Table 2 were determined using centroid tracking of debris, and the directivity characteristics were derived from the histograms in Fig. 10, making them relative to the tornado's location.

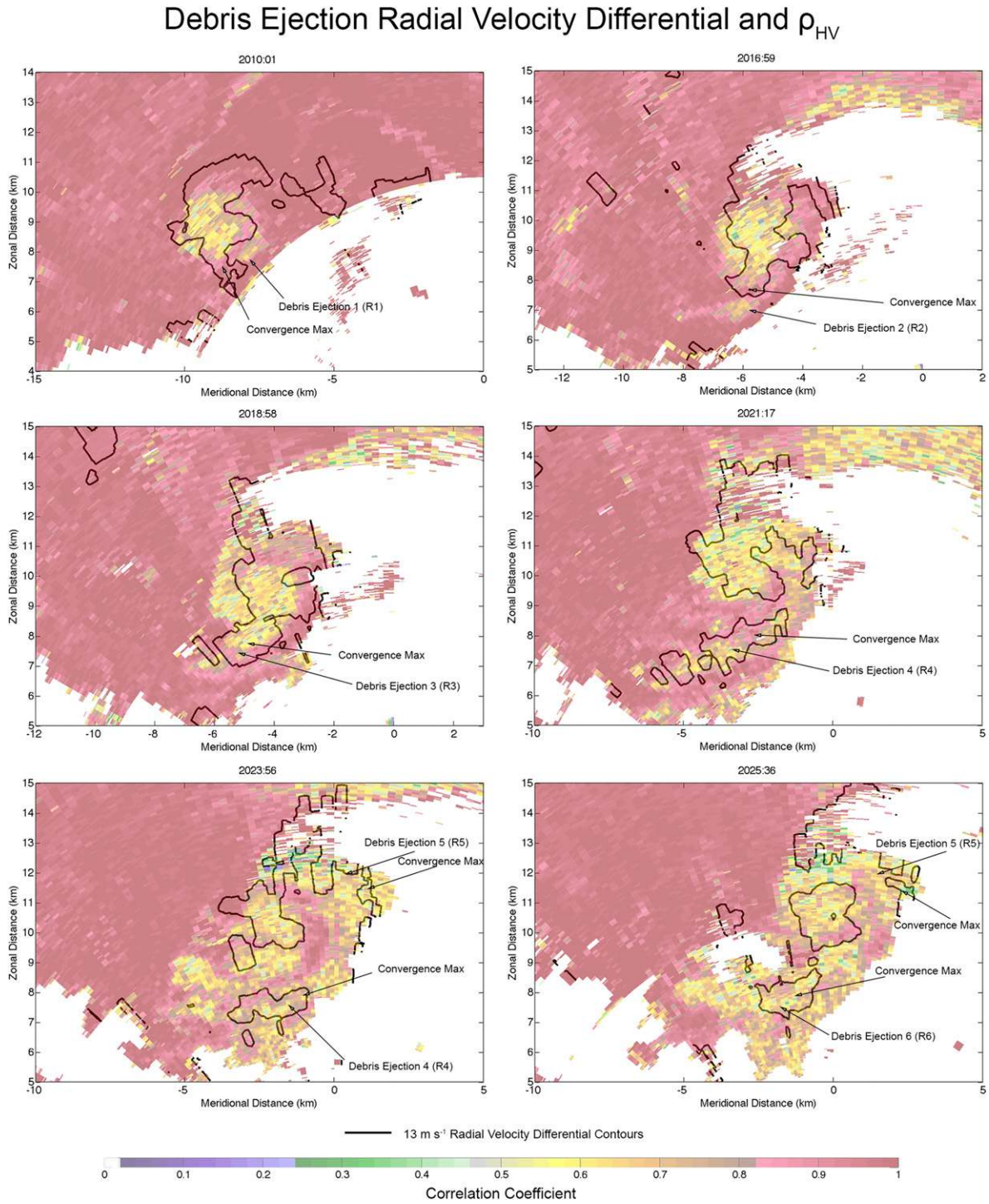

FIG. 7. Comparison of the first six debris ejections with single-Doppler PX-1000 maximum radial velocity increase field (v_i). Shading is PX-1000 ρ_{HV} and solid lines are 13 m s^{-1} v_i contours. Areas of convergence maxima corresponding with each debris ejection are marked by arrow and text. Distances labeled are from the radar location, which is to the south of the frame. Note that the first two ejections have significant cross-beam components, making them less obvious in the v_i field.

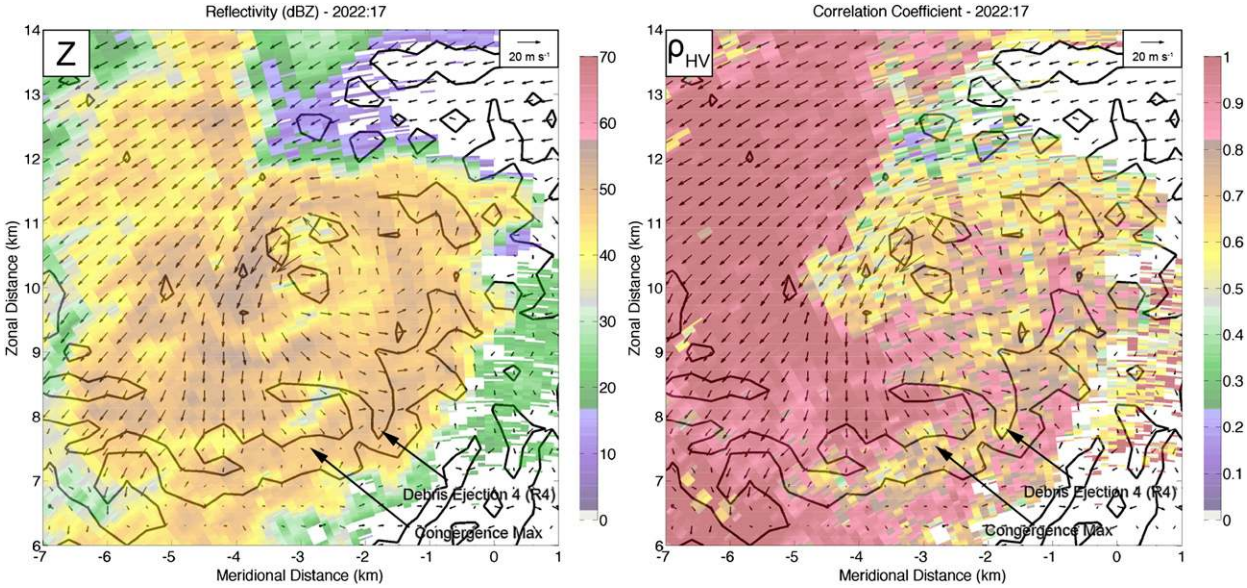

FIG. 8. Sample dual-Doppler analysis from PX-1000 and the KTLX WSR-88D. Overlays are two-dimensional ground-relative wind vectors and 0.1 s^{-1} horizontal convergence contours. Underlays are (left) PX-1000 Z_{HH} and (right) PX-1000 ρ_{HV}. Time of the analysis is 2022:17 UTC, and the axes are labeled with respect to the PX-1000 location, which is to the south of the frame. KTLX is located to the right of the frame.

As shown in Fig. 10, it is apparent that R4, R5, and R6 contain nearly an order of magnitude more radar gates with debris than did the other RFGFSs. This may be due to stronger surges, but it may also be due to more debris available for lofting/fallout. These particular RFGFSs are discussed in depth in the subsequent subsection, but it is worth noting that R4–R6 occur with starting points occurring approximately every 1.6 min. The starting time difference of all the RFGFSs, however, ranges from 6.3 (R1–R2) to 1.0 min (R5–R6). During times other than the occlusion/loop period, described in section 4c, this disparity is much smaller, with times ranging from 6.3 (R1–R2) to 3.0 min (R2–R3), and an average of 4.5 min. Despite the lack of direct correlation between the RFGFSs and the track shifts in Figs. 5 and 9, a number of the track shifts did occur during or just after a RFGFS. This is visible after R1, R2, the loop after/during R5 (described in section 4c), and shortly after R7. RFGFS R8 also preceded a final occlusion.

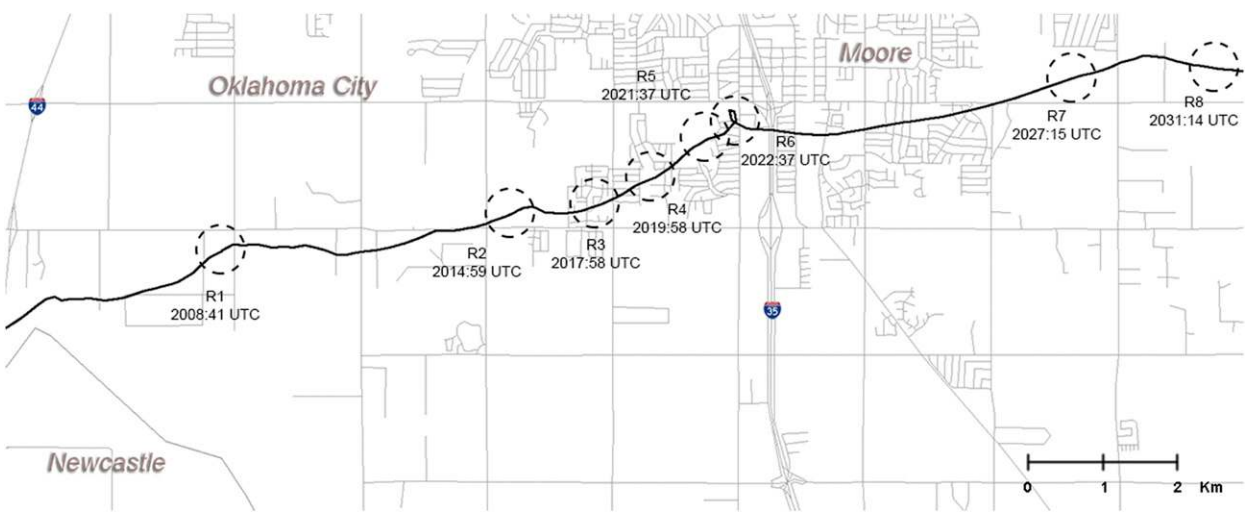

FIG. 9. PX-1000 tornado center track (solid black line) and timing/location of eight RFGFSs (labeled R1–R8 with dashed circles denoting the location along the track). Noted times and locations are the *beginning* of each surge.

TABLE 2. Rear-flank gust front surge characteristics.

RFGFS	Time begin (UTC)	Time end (UTC)	Max velocity ($m\,s^{-1}$)	Primary direction*
R1	2008:41	2010:01	18.1	116° (ESE)
R2	2014:59	2018:38	13.4	206° (SSW)
R3	2017:58	2020:18	13.6	206° (SSW)
R4	2019:58	2023:36	11.6	223° (SW)
R5	2021:37	2026:55	18.7	75° (E)
R6	2022:37	2026:55	26.4	184° (S)
R7	2027:15	2028:55	20.1	152° (SSE)
R8	2031:14	2032:54	19.0	137° (SE)

* Relative to the tornado.

c. *Loop at Moore Medical Center and late track*

Shortly after the damage survey presented in Burgess et al. (2014) was completed, there were questions regarding whether a loop or a cusp had occurred near the MMC, approximately 450–500 m west of I-35 (G. J. Stumpf 2013, personal communication; Atkins et al. 2014a). PX-1000 data were used to confirm that the tornado had in fact moved in a circular path just west of the MMC. However, the exact path of the circulation in the PX-1000 data was offset slightly from the damage path (Fig. 11). The difference is on the order of 30 m in each direction and is possibly due to a combination of the wide native beamwidth of PX-1000, the potential for vortex tilting (French et al. 2014), and the effects of combined translational/rotational wind components. Between the time of 2021:37 and 2023:17 UTC, the tornado completed a counterclockwise loop that spanned a total length of approximately 0.5 km with little forward progress. This event can be seen in the time series data of forward ground speed and direction in Fig. 5 as the tornado moved in a northeast to north to southeast direction at a speed as low as $3\,m\,s^{-1}$. At the same time, Δv_r values dipped from a previous high of nearly 125 to $75\,m\,s^{-1}$ in the span of less than 150 s. Shortly after the looping motion in the track, an increase in forward ground speed was observed, from 3 to $21\,m\,s^{-1}$ in 4 min. During this time, despite the still heavily populated area, damage indicators generally lessened, with the maximum damage observations dropping to EF3 for the first time in 12 min.

Although the loop at MMC is apparent in the PX-1000 data, there were a number of potentially related changes in storm structure observed in the minutes beforehand. To detail these changes, four sampling times have been selected for annotated presentation in Fig. 12, spanning from 2016:39 to 2026:16 UTC. These times are marked in Fig. 11 for reference along the track. Prior to 2016 UTC, a relatively mature tornado in a pseudo–steady state had been ongoing for approximately 20 min (Fig. 2), aside from two minor RFGFS and track shift

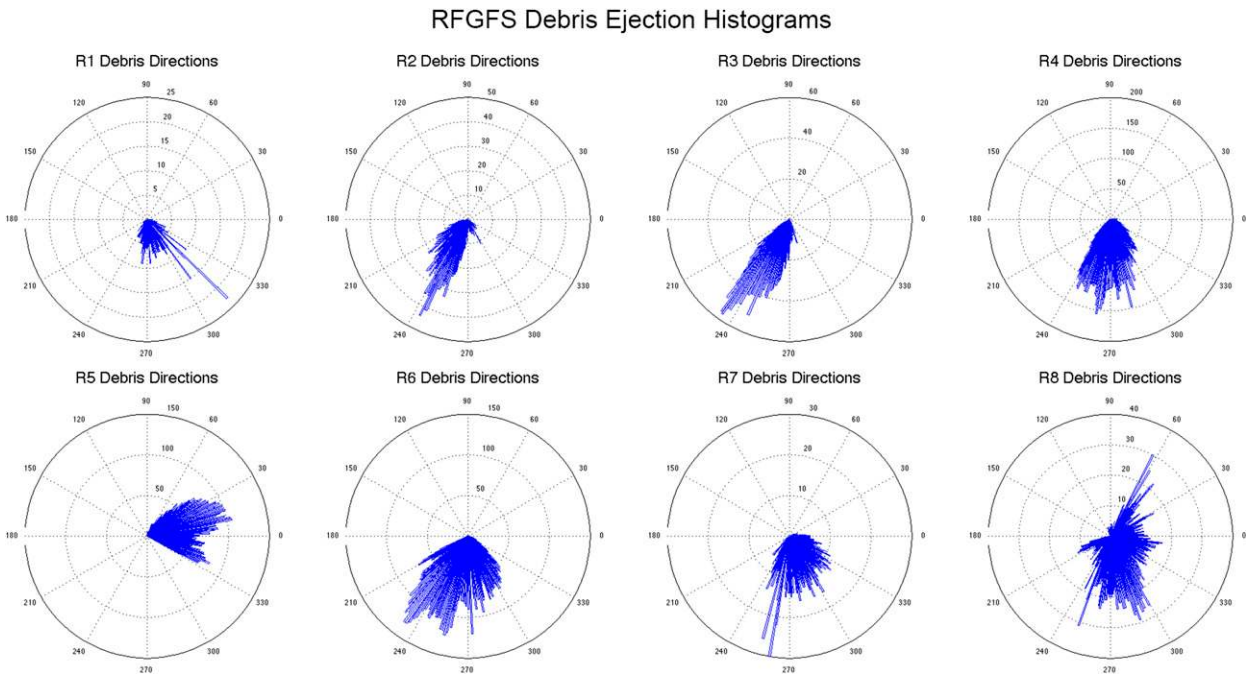

FIG. 10. Polar coordinate histograms of radar gates containing debris and their location relative to the center of the tornado (in a moving reference frame) for RFGFSs R1–R8. Magnitude is marked radially outward by number of gates, and direction (360 1° bins) indicates relative debris trajectory direction from the tornado. Each ejection plot is normalized by the number of gates, meaning the radial dimension changes from plot to plot.

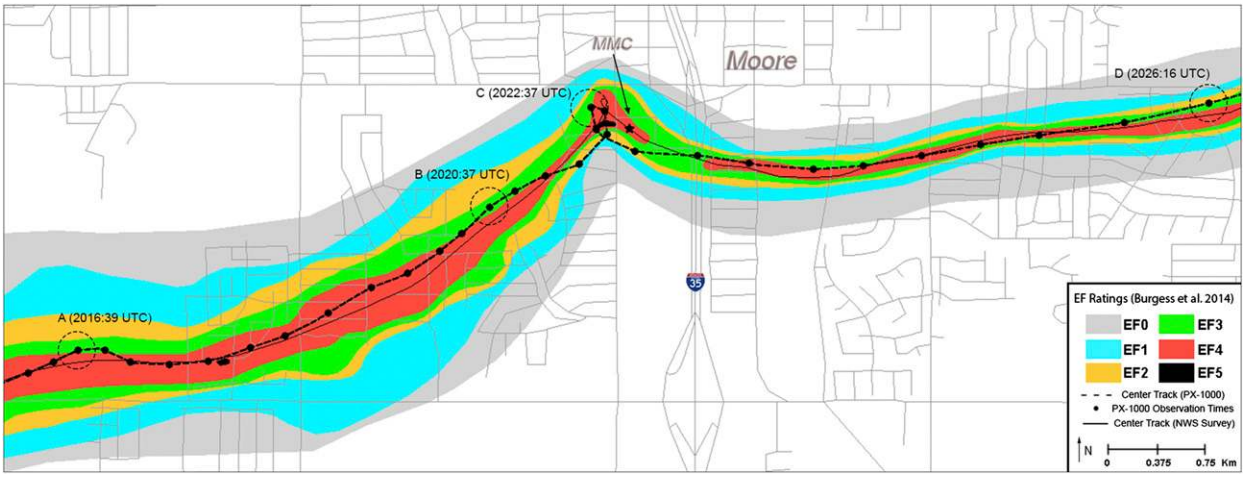

FIG. 11. EF-scale damage ratings [colored shading, from Burgess et al. (2014)], vortex center track from PX-1000 Δv_r data (dotted black line), and NWS damage survey center track (thin solid black line) for the loop area near the MMC (black star). Circled/labeled times A–D refer to the data presented in Fig. 12.

events (Fig. 5). Additionally, a distinctive Z_{DR} arc was evident from the forward flank, all the way to the base of the hook and around the TDS. Between 2014 and 2017 UTC, an area of high Z_{HH} (~60 dBZ), high Z_{DR} (~5 dB), and low ρ_{HV} (~0.9) broke off from the rear/forward-flank downdraft interface north of the tornado and surged southward along the RFGF at a speed of 29 m s^{-1}. This phenomenon will be referred to as a "southern surge" from this point forward, and is similar to observations by Kumjian (2011) and French et al. (2015).

The final stage of this southern surge can be seen in Fig. 12a. At this time, 2016:39 UTC, a strong v_r couplet, quasi-circular tornadic debris signature, and Z_{DR} arc were apparent as the mature tornado continued. At nearly the same time as the completing surge, the first area of EF5 damage occurred near Briarwood Elementary School, 2.75 km southwest of MMC. This period marked a distinct turn to the north-northeast, as indicated by the track in Fig. 11 and the vortex direction time series in Fig. 5. In the forward flank, ρ_{HV} was relatively high, indicating primarily rain, but an area of lowered Z_{DR} was beginning to break into the Z_{DR} arc along the southern fringe of the forward-flank downdraft (FFD).

Shortly afterward, at 2020:37 UTC, the lowered Z_{DR} values in the forward flank showed a transition to the west (in a storm-relative sense), within the portion of the Z_{DR} arc closest to the updraft (Fig. 12b). This has been hypothesized by Kumjian et al. (2010) to indicate a disruption in the updraft and an occlusion process. Additionally, a large area of low ρ_{HV} was becoming evident on the southern flank of the FFD, possibly indicating debris fallout (Magsig and Snow 1998). Subsequently, the southern surge passed through the RFD, and resulted in a RFGFS (R4) and an associated debris ejection, visible in both Z_{HH} and ρ_{HV} in Fig. 12b. In the wake of R4, a distinct break in the hook echo to the northwest of the tornado became evident. The high Z_{DR} values in the southern surge had transitioned to lower values as debris was mixed in with the RFGFS, and the couplet had maintained its high Δv_r over the period (nearly 125 m s^{-1}, among the highest values during the tornado). As can be seen in Fig. 10, R4 maintained a predominantly southern motion. Additionally, a strong northerly shift in the track was well under way.

Two minutes later, at 2022:37 UTC, the lowered Z_{DR} values had mostly filled in across the southern forward flank, but an area of lowered Z_{DR} had become apparent to the west of the hook (Fig. 12c). In the same area, a seemingly disrupted hook structure is present in Z_{HH}. The low ρ_{HV} intrusion in the FFD had shrunk in size but was still evident. A second and third RFGFS (R5 and R6) became evident in both Z_{HH} and ρ_{HV}, and the Δv_r had lowered from 125 to 100 m s^{-1}, indicating a weakened couplet in v_r. RFGFS R5 displayed intensity and directional characteristics of an occluding RFD surge typically seen in occluding cyclic mesocyclogenesis (Fig. 10; Adlerman and Droegemeier 2005), with large components of the debris ejection pointing to the northeast, possibly indicating an attempted occlusion of the tornadic circulation as RFD air began to cut off the inflow air to the southeast. RFGFS R6, on the other hand, was oriented to the south, in a similar fashion to earlier RFGFSs. At this point, the tornado slowed to under 5 m s^{-1} and began to move toward the northwest, also a common characteristic of an occluding mesocyclone/tornado (Burgess et al. 1982; Adlerman et al. 1999; Dowell and Bluestein 2002a).

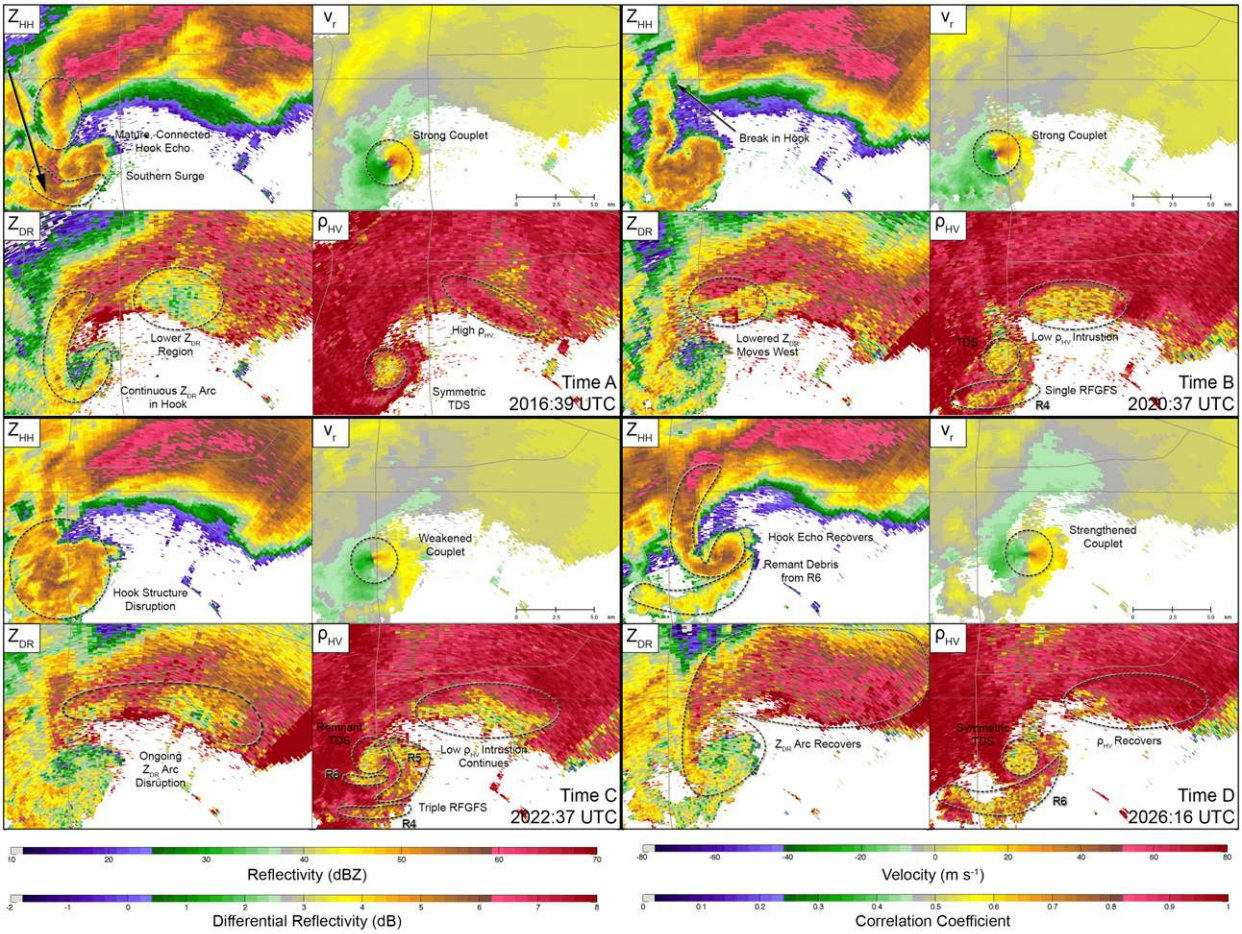

FIG. 12. Sample Z_{HH}, v_r, ρ_{HV}, and Z_{DR} data (clockwise from top left in each subframe) from different times/locations during the tornado loop period. Times are in reference to circles and times A–D in Fig. 11.

At 2026:16 UTC (Fig. 12d), R6 had surged quickly southward and was arguably the strongest of the RFGFSs (26.4 m s^{-1}; Table 2) and had primary debris ejection trajectories toward the south and south-southwest (Fig. 10). While the selected time of observation was past the time of the loop, it clearly shows the debris associated with R5 being ejected to the northeast of the tornado while R6 surges to the south. At this time, the forward ground speed had increased to 9 m s^{-1} (Fig. 5). Additionally, both the lowered Z_{DR} and ρ_{HV} values had recovered to the values seen during the mature stages before the loop. The Z_{DR} arc, specifically, had recovered to a fully mature state, and the hook echo was once again fully connected in Z_{HH}. A nearly symmetric TDS is evident in ρ_{HV}, and the remnant debris tail from R6 (and presumably previous RFGFSs) is clearly visible in all moments.

Shortly prior to the recovery shown in Fig. 12d, at 2024:16 UTC, a fully formed double RFGFS structure was evident. Annotated selections of R5 and R6 are presented in Fig. 13, with solid arrows showing mean debris motion along each surge. Forward ground speed rapidly increased to 15 m s^{-1}, even reaching as high as 21 m s^{-1} between 2026 and 2027 UTC. Afterward, between 2027 and 2032 UTC, Δv_r was maintained in the 60–70 m s^{-1} range as forward ground speed recovered to ~10 m s^{-1} and the maximum EF-scale damage ratings fluctuated between EF4 and EF2. A RFGFS (R7) and an associated track shift occurred at 2027:15 UTC, and a final RFGFS (R8) with predominantly easterly ejection of debris indicated a final occlusion and tornado dissipation. The tornado moved its final 8 km (postloop) in 12 min, after it had traversed 15 km in 27 min.

5. Discussion

The RFD structure in a supercell (Lemon and Doswell 1979) has been hypothesized to be at least

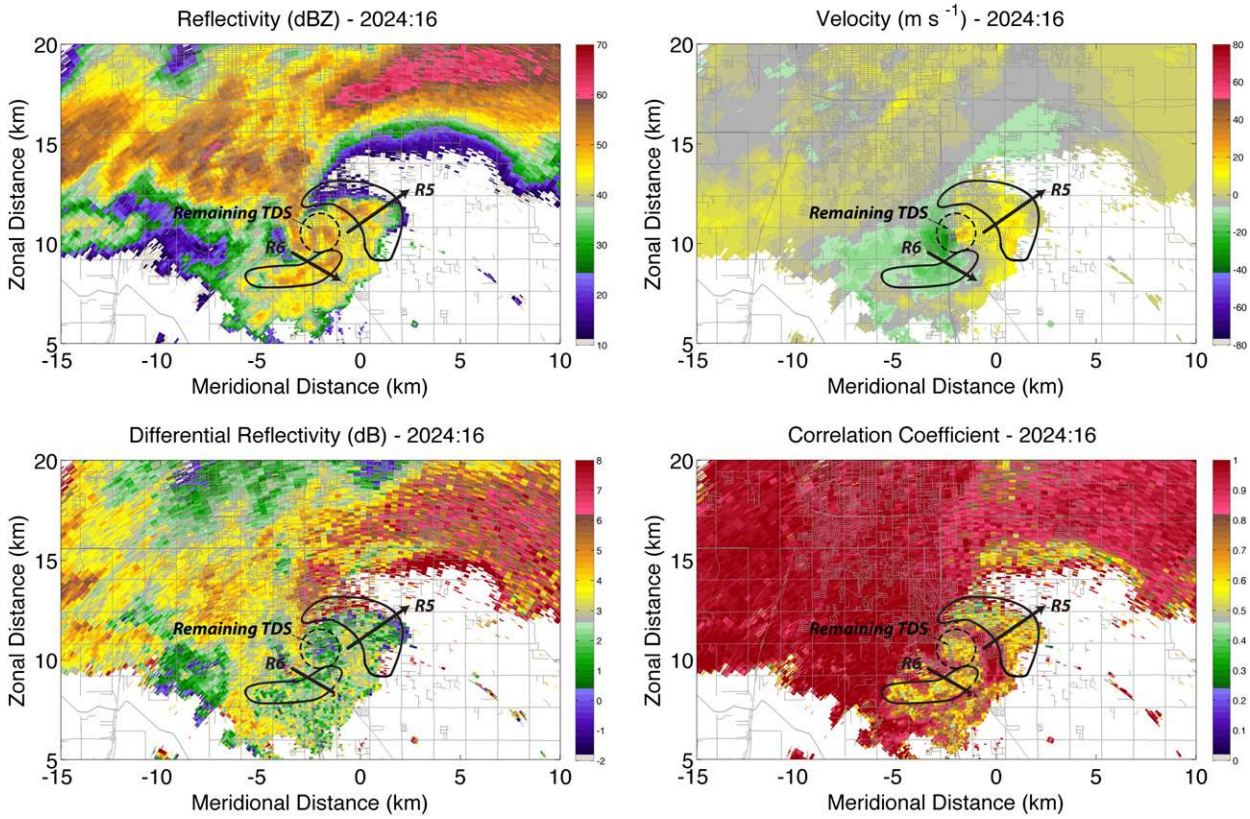

FIG. 13. (from top left, clockwise) PX-1000 Z_{HH}, dealiased v_r, ρ_{HV}, and Z_{DR} at 2024:16 UTC. Annotations and thick lines mark debris ejection 1 (R5), and debris ejection 2 (R6) in the failed occlusion process (Fig. 14). Thick arrows depict approximate predominant path of debris ejections/RFGFSs. The dotted circle in each panel marks the TDS remaining after debris ejections.

partially responsible for both tornado maintenance (Marquis et al. 2008) and eventual tornadic decay through the occlusion process of cold outflow air moving from the south and west sides of the updraft/tornado, around to the north and east sides (Brandes 1978; Lemon and Doswell 1979; Markowski 2002; Marquis et al. 2012). It has been proposed that the particular RFD surge that results in tornadic occlusion cuts off the source of warm inflow air, disrupting the updraft maintenance process (Klemp and Rotunno 1983; Wicker and Wilhelmson 1995; Adlerman et al. 1999). However, it is important to note that Marquis et al. (2012) show that some tornadoes do not occur until after occlusions.

It can be seen in the PX-1000 data presented that a nonstandard mode of cyclic mesocyclone behavior was evident during and around the time of the loop. To date, the majority of cyclic processes observed during similar events revolve around cyclic mesocyclogenesis and/or tornadogenesis. Cyclic mesocyclogenesis can be broken into occluding and nonoccluding modes (Adlerman and Droegemeier 2005). In the occluding mode, as each mesocyclone occludes toward the rear side of the storm, a new mesocyclone forms downshear along the trailing RFGF (Ziegler et al. 2001; Beck et al. 2006; French et al. 2008). In the nonoccluding mode, the existing mesocyclone propagates away from the main body of the storm along the RFGF as a new mesocyclone forms nearer to the main hook echo. Cyclic tornadogenesis, on the other hand, assumes that in addition to cyclic mesocyclogenesis, new vorticity maxima must form along the RFGF at low levels, increasing in magnitude with height (Dowell and Bluestein 2002a). This concept builds on the Burgess et al. (1982) concept to describe observations of some mesocyclones throughout a storm's lifetime producing relatively short-lived cyclic tornadoes (Dowell and Bluestein 2002b; Tanamachi et al. 2012).

Furthermore, multiple cyclic tornado cases have observed dissipating tornadoes to move along or near to the occlusion point, resulting in motion toward the "rear" of the updraft (Dowell and Bluestein 2002a; Houser 2013). In some cases, this has led to a nearly full loop of the tornado before eventual occlusion and dissipation occurs (Wurman et al. 2007; Bluestein et al. 2010; Tanamachi et al. 2012). Houser (2013) and Houser et al. (2015) show a hybrid case from 24 May 2011 in

which it is postulated that the RFGFS remained contained without fully wrapping around the updraft, allowing the reorganizing mesocyclone to keep access to warm inflow air. While this did allow the tornado to continue without immediate occlusion, dissipation did occur shortly thereafter.

The Moore case is distinctive in that the occluding RFGFS occurred during a period of rapid, cyclic RFGFS generation, resulting in a well-timed interaction between multiple RFGFSs that caused unusual behavior of the parent mesocyclone and associated tornado. The existence of these observations on such short time scales means that high-temporal resolution observations at high spatial resolution were necessary to observe separation between individual RFGFSs. Although dual-Doppler observations on the same resolution scales would be ideal, the use of polarimetric radar and associated debris ejections leads to the inference that 8 RFGFSs occurred over a 23-min period. It is important to note that these RFGFSs appear to be manifestations of concentrated RFD flow. There could certainly be dynamic and/or thermodynamic forcing causing multiple areas of focus within the RFD that we are not able to quantify. This has been suggested by Skinner et al. (2014), where dual-Doppler analysis at high-temporal resolution showed multiple areas of concentrated downdrafts within the RFD. However, other than these observations, the existence of such high-resolution surges is lacking in the literature.

While the term ''ejection'' was chosen for these observations, it should be noted that the predominant forcing resulting in the debris' existence in a tail shape is not necessarily known. Because of the lack of a symmetric ejection of debris, a *purely* lateral ejection caused solely by centrifuging is an unlikely scenario, but some combination of centrifuging, debris fallout, and convergence along the RFGF is a likely culprit. Additionally, observations of RFGFSs at such high frequency is rare, however, recent studies such as Skinner et al. (2014) have seen comparable time scales using relatively rapid-scanning dual-Doppler data. Additionally, the only known observations of debris tails/ejections (Houser 2013; Houser et al. 2015) occurred in another EF-5 storm and were collected at the X band. It is possible that such observations will become more prevalent in the near future as rapid-scanning polarimetric radar (especially at short wavelengths such as the X and Ka bands) become more ubiquitous in the field.

It is thought that the high frequency of RFGFSs around the occlusion/loop period may have to do with the weakening/occluding mesocyclone, but it is not clear that there is a direct relation. These relatively quiescent periods display an unmistakably periodic nature of the RFGFSs, although cyclic mesocyclogenesis and/or cyclic tornadogenesis do not occur. It should be noted that in some cases, the debris ejection signatures appear to lead the convergence signatures (or at least line up with each other). Since the observations of PX-1000 are quite high (i.e., hundreds of meters), the position of the gust front is likely further ahead near the surface. The debris lofted into the beam may, therefore, be associated with the head of a density current that is surging forward below the radar beam. Additionally, a number of causal factors related to the RFGFSs may have affected the tornado track; however, without rapid volumetric scanning capabilities, it is unclear whether these occurrences are due to vortex tilt or other factors. The possible correlation between RFGFSs and track shifts is intriguing, but reasons for these shifts are beyond the scope of this research.

As a potential explanation for what occurred in the Moore tornado, a hybrid conceptual diagram, adapted from the combination of PX-1000 data, Burgess et al. (1982), Dowell and Bluestein (2002a), and the Houser (2013) case, is presented in Fig. 14. As the RFGFS associated with the occlusion (RFGFS 1) wraps RFD air around the updraft and tornado, weakening the mesocyclone and associated vorticity, the tornado begins to move to the north and eventually the northwest in an occlusion-type pattern. Near the apex of the northward turn, a secondary RFGFS, labeled RFGFS 2 in the diagram, pushes a new corridor of RFD air toward the south and southeast, in stark contrast to the predominant direction of RFGFS 1. This process may or may not result in a full loop (a cusp track would also be conceivable), and could take place with more than two RFGFSs. RFGFSs 1 and 2 in the diagram are analogous to R5 and R6 in the Moore case (Fig. 13).

The prevailing hypothesis is that initially, an imbalance of inflow and RFD winds causes the tornado to move north, similar to an occlusion process. However, with the strong southerly surge directly afterward, the inflow and RFD wind balance changes and the vortex migrates southward, restoring the location of the tornado in the updraft and preventing the occlusion of the tornado. This is similar to the tornadic mesocyclone cases described in Adlerman and Droegemeier (2005) and Houser (2013); however, the tornado and mesocyclone recover fully and continue on a path similar to that before the original northerly turn and in a relatively mature state. Additionally, depending on the strength, timing, and directivity of the secondary RFGFS, as well as any additional RFGFSs throughout the process, abrupt changes in forward ground speed may be observed, as with the Moore case just past I-35.

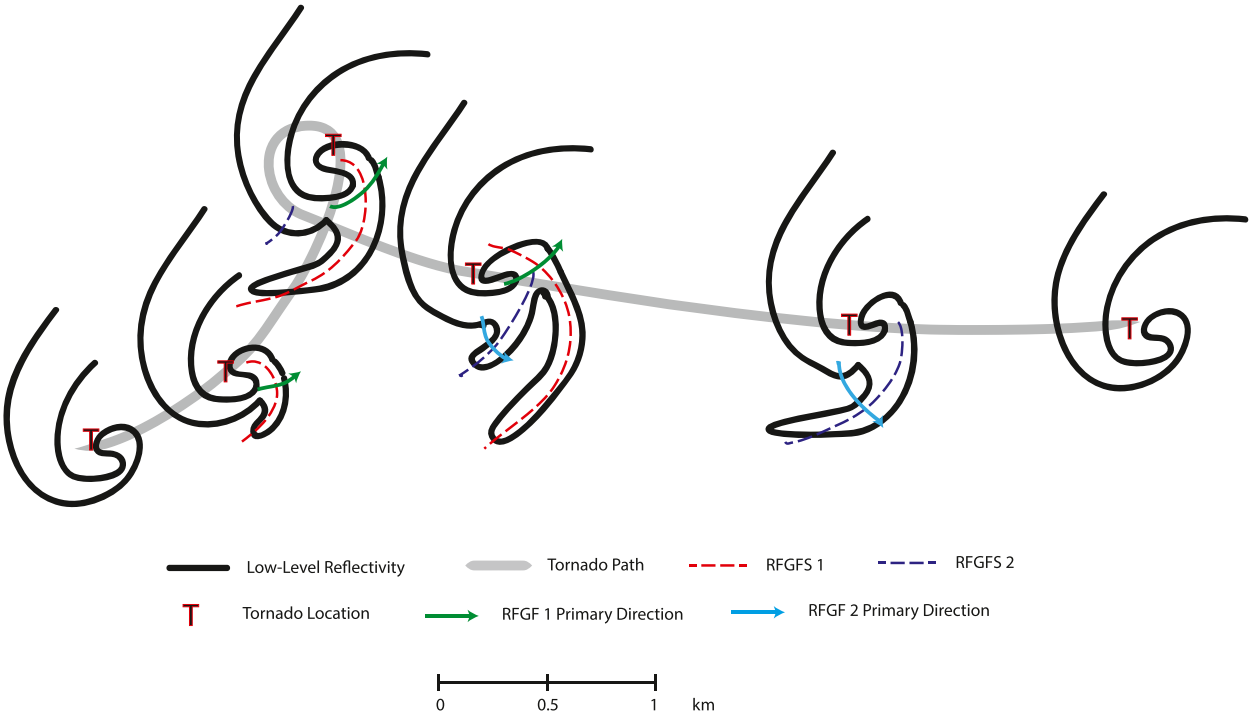

FIG. 14. Conceptual diagram of the failed occlusion process. The tornado and mesocyclone are first impacted by an occlusion-forcing RFGFS (RFGFS 1), which wraps around the tornado, causing a turn to the north. A second RFGFS (RFGFS 2) impinges upon the tornado near the apex of the loop with a predominantly southern direction relative to RFGFS 1, causing the tornado to move in a circular pattern and regain a steady state after a looped track. RFGFSs 1 and 2 are analogous to R5 and R6, respectively, in the Moore case.

It is important to note that the origins of R5 are not as readily known as the other RFGFSs because of its orientation to the north and east. While it would be a relatively rare occurrence for the RFD to undercut the updraft region of the storm, the possibility of the RFD wrapping *around* the updraft/tornado regions should be noted [i.e., similar to a synoptic-scale occlusion process; see Fig. 7 in Kumjian (2011)]. RFGFS R5 appears to be related to the original source of R4 (the ''southern surge''), but a distinct break and difference in debris trajectory is evident. The possibilities for debris sources include RFD wrap around, forward-flank debris fallout, and pure tornadic vortex debris fallout (during a distinct weakening stage), and if more dual-Doppler data were available, the possibility of an occlusion downdraft could also be explored.

We are referring to this process as a ''failed occlusion'' of the parent mesocyclone and tornado because of the apparent occlusion processes observed prior to the loop. As shown in Fig. 12, a number of events indicative of a weakening updraft, debris fallout, and an attempt at occlusion are evident. The southern surge of precipitation that preceded the northerly turn (2016:39 UTC; Fig. 12a) was followed by *single-elevation* observations of lowered Z_{HH} and Z_{DR} (2020:37 UTC; Fig. 12b), possibly indicating fallout of large drops to heights lower than the radar beam elevation that were then transported rapidly south by the RFD. Such a development in the RFD would likely lead to an enhanced area of RFD winds, resulting in a RFGFS as indicated shortly after in R4. This hypothesis is also supported by the relatively high values of Z_{HH} and Z_{DR} in the southern surge (Fig. 12a).

It is hypothesized that the driving force behind the relatively large/strong RFGFS R4 was a combination of more availability of debris (i.e., structure density) and the downward momentum generated in the southern surge via precipitation loading in a wet downdraft. It is important to note that the southern surge is a manifestation of a three-dimensional process, and the polarimetric values associated with the southern surge are likely a result of predominantly large raindrops falling through the RFD, possibly mixed with small debris or nonuniform beam filling (Herzegh and Jameson 1992; Ryzhkov and Zrnić 1995; Kumjian and Ryzhkov 2008; Kumjian et al. 2010). As the large drops fell through the radar beam, it is believed that they were caught in the strong southern surge, transporting

them to the southern portion of the RFGF as part of a developing RFGFS.

Eventually, this process appeared to result in a disruption of the hook in Z_{HH} and the Z_{DR} arc. It has been suggested by Kumjian (2011) that the appearance of low values of Z_{DR} to the west of the hook may be indicative of an occlusion downdraft. Additionally, the Z_{DR} arc disruption occurred close to the time that would be expected in an occlusion of the parent mesocyclone and/or tornado (Kumjian et al. 2010; Crowe et al. 2010; Palmer et al. 2011). After the loop, a clear recovery in the Z_{DR} arc is evident by high values of Z_{DR} fully connected around the updraft and hook echo. To emphasize the difference between the early mature stages of the tornado, the loop time, and the later mature stages of the tornado, Fig. 15 shows Z_{HH}, ρ_{HV}, Z_{DR}, and differential propagation phase (ϕ_{DP}, in °) at three times during the tornado. The difference in Z_{DR} arc connection and Z_{DR} values in the forward flank are clear in the middle column compared to the left and right columns.

Despite the attenuation correction applied to the PX-1000 data, and in order to rule out attenuation as a cause for the hook echo break and the area of lowered Z_{DR}, KTLX WSR-88D data are presented in Fig. 16. KTLX was located 20 km northeast of PX-1000, and was scanning in volume coverage pattern 12 (Brown et al. 2005). The data in Fig. 16 are from the 1.4° scan in order to closely match the height of the PX-1000 beam. Numerous similar features can be seen, albeit at lower spatial and temporal resolutions. It should be noted that Z_{HH} values in the KTLX data along the southern periphery of the forward flank are low enough to suggest that the low ρ_{HV} values in PX-1000 may not be a result of hail core fallout; rather, that debris fallout is a possible explanation. While sparse, large hail cannot be ruled out, the KTLX observations at least suggest that debris fallout is plausible, especially when the amount of debris available for fallout (in a well-developed area) is considered. At no other point in the KTLX data was any indication of a Z_{DR} arc disruption seen.

Additionally, it can be speculated that the intrusion of low Z_{DR} and ρ_{HV} values into the southern part of the FFD indicate the potential for a weakening updraft. Magsig and Snow (1998) suggest that rapid weakening of the updraft in a strong tornado could lead to debris fallout in the FFD region. Even small debris mixed with raindrops would be noticeable in both Z_{DR} and ρ_{HV} fields. The difference between low Z_{DR} and ρ_{HV} intrusions in the middle column of Fig. 15 is clear compared to the pure rain (and size sorting mechanism of the Z_{DR} arc) in the left and right columns, further indicating a weakened updraft and possible occlusion attempt.

The distinct pattern of debris ejecting to the northeast along the occluding RFGFS, combined with the observations of the tornado moving toward the north in the PX-1000 data, corroborates the hypothesis that an occlusion process was under way. However, visual observations from numerous sources of a continuous condensation funnel and tornado, as well as a continuous damage swath and no indication of a new couplet center in the PX-1000 data suggest that the same tornado was maintained after the loop. The limited number of dual-Doppler analysis points with KTLX, as well as discussions with collaborators looking at other datasets, also suggests that only one mesocyclone existed throughout the failed occlusion process. Despite the highly dynamic and changing situation, even 20-s updates may not be enough data to determine without a doubt that only one updraft was present throughout the occlusion process. It should be noted that while the failed occlusion is one hypothesis, other options for mesocyclone/updraft evolution certainly exist with this case (such as extremely rapid cyclic mesocyclogenesis, multiple tornadoes, and/or additional updrafts).

Despite the reduction in apparent strength, the area near MMC was one of only two primary areas where EF5 damage indicators were found in the Atkins et al. (2014a) and Burgess et al. (2014) studies (Fig. 11). While this area is highly populated, the slow speed of the tornado over a small spatial area could have had significant impacts on resulting damage (e.g., see Snyder and Bluestein 2014). Although enhanced damage is possible due to extended periods of high wind speeds, this area was also in a more-developed subdivision (Burgess et al. 2014), so no concrete conclusions can be drawn regarding such a correlation.

Finally, the polarimetric variables of the RFGFSs are relatively consistent with each other, as well as those seen in TDSs (Bodine et al. 2013). A summary of the polarimetric variable distributions in the eight RFGFSs is presented in Fig. 17. The primary difference between RFGFS observations and those expected in a TDS is the higher median of Z_{DR}. This is likely due to two factors: 1) the existence of more rain drops in the RFGFS where centrifuging is not a primary driving factor of size sorting, and/or 2) debris fallout with a common alignment orientation due to strong, straight-line winds. Additionally, ρ_{HV} median values are slightly higher than those seen in Bodine et al. (2013). One would assume that the higher frequency of PX-1000 (X band as opposed to S band) would tend to lead to lower ρ_{HV} values due to the greater electrical sizes of debris; however, the higher values could be due to the effects of rain and smaller debris being lofted, resulting in less resonance scattering effects. Also of note is an apparent negative mean in Z_{DR} in the TDS (not the debris ejections; not

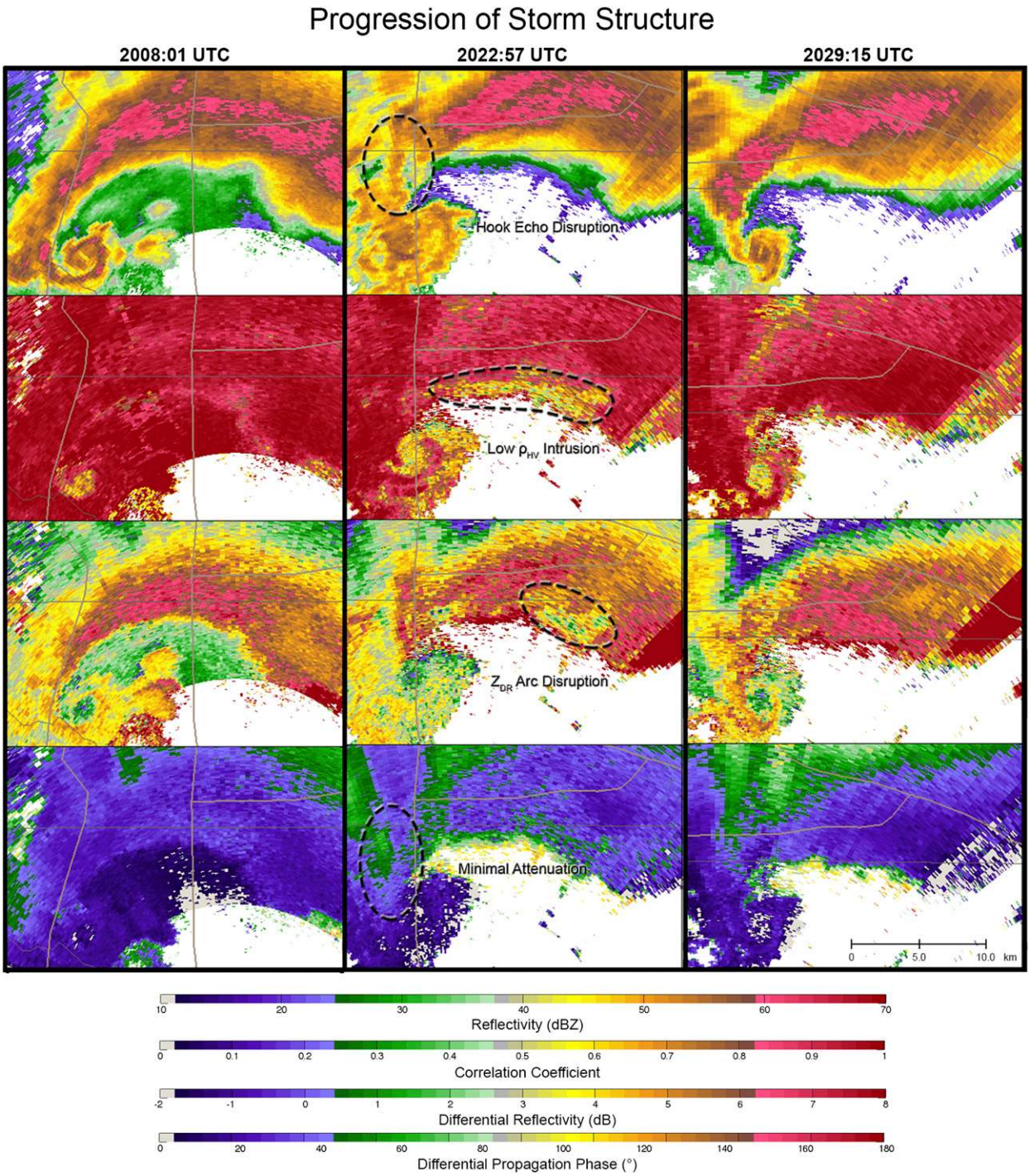

FIG. 15. (from top to bottom) PX-1000 Z_{HH}, ρ_{HV}, Z_{DR}, and ϕ_{DP} at (from left to right) 2008:01, 2022:57, and 2029:15 UTC. (left),(right) Mature reflectivity, TDS, and Z_{DR} arc are in stark contrast to those in the (middle) near/during the loop at MMC.

shown), a phenomenon discussed by Ryzhkov et al. (2005) and Bodine et al. (2014). This phenomenon is a manifestation of Mie scattering and common debris alignment, but could also be caused by differential attenuation; this is an area of ongoing research.

6. Conclusions

The 20 May Moore tornado is a high-profile meteorological case that was observed by PX-1000 at high temporal resolution, allowing for a fine-grain analysis

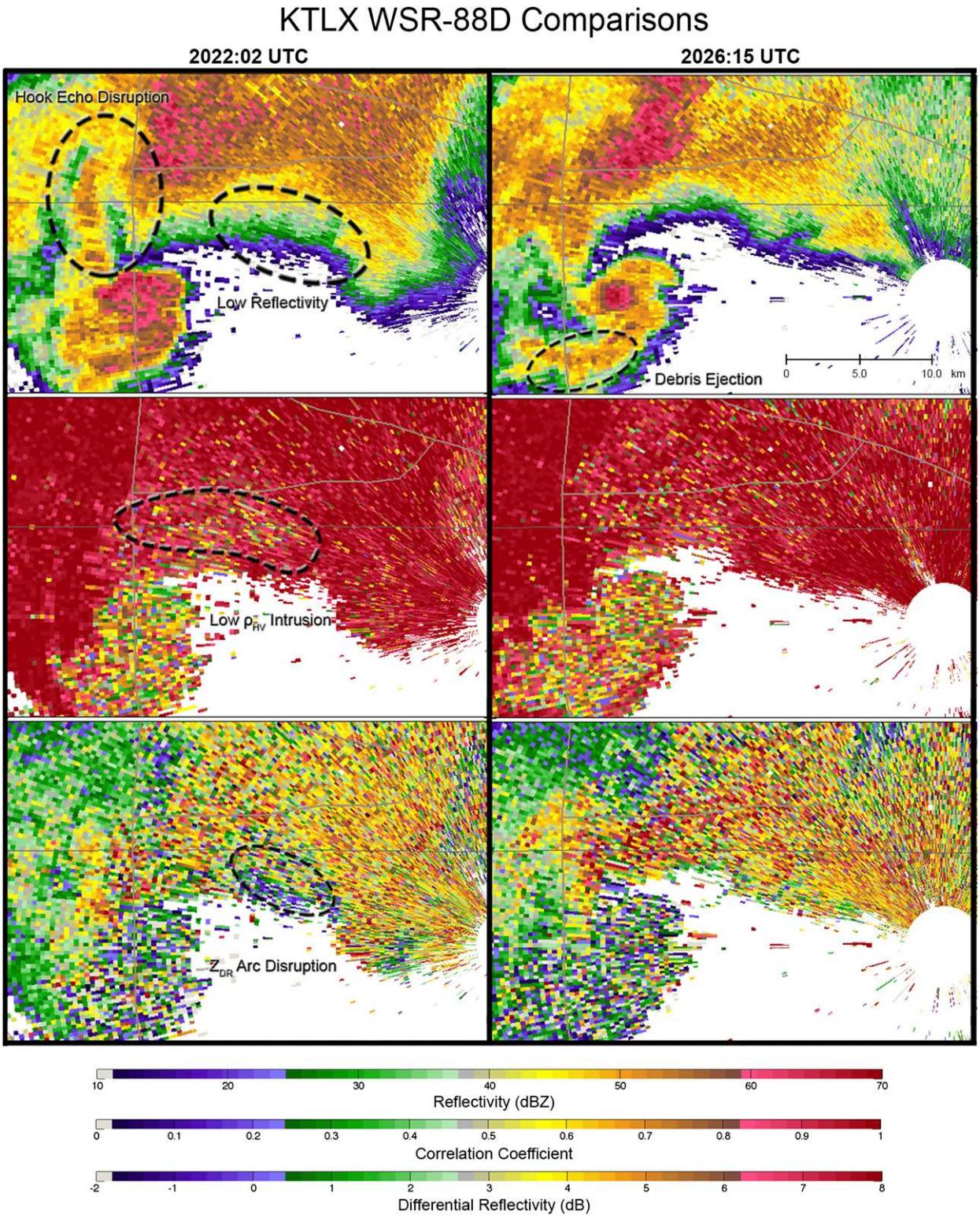

FIG. 16. (from top to bottom) KTLX Z_{HH}, ρ_{HV}, and Z_{DR} at (from left to right) 2022:02 and 2026:15 UTC. Notable similarities with PX-1000 including hook echo and Z_{DR} arc disruption, low ρ_{HV} in the forward flank, and a debris ejection following the loop are marked. KTLX data are from the 1.4° tilt.

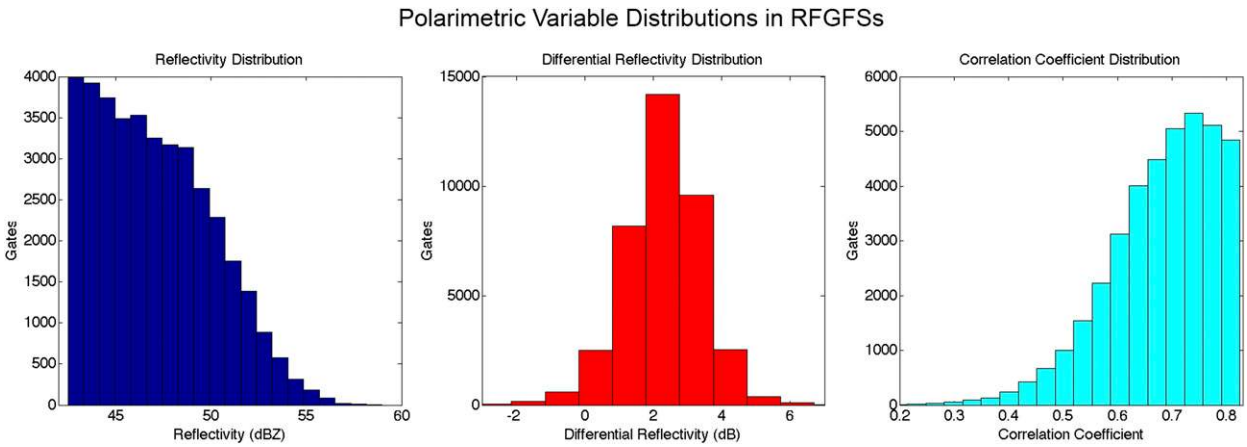

FIG. 17. (from left to right) Total distribution of Z_{HH}, Z_{DR}, and ρ_{HV} moment estimates within the eight RFGFSs, R1–R8.

of various storm attributes that occurred on rapid time scales. While dual-Doppler, volumetric observations at a similar temporal resolution would allow for full analysis of the various RFGFS structures, the lack of such observations requires the use of polarimetric estimates to track RFD velocities and directions. Through this analysis, eight different RFGFSs marked by distinct debris ejection patterns were identified during the lifetime of the tornado; additionally, *all* of the RFGFSs visible in v_r data were associated with a debris ejection. Among the eight RFGFSs, three occurred in rapid succession, including the middle RFGFS that marked an apparent occlusion process with a debris ejection primarily angled to the northeast.

During the ongoing occlusion process, a second RFGFS aligned primarily to the south appeared to have provided enough balance between the supercellular inflow and outflow regimes to maintain the dominant mesocyclone and tornado structure, effectively "pushing" the tornado back onto an easterly path after the completion of a counterclockwise looping trajectory. Afterward, a significant increase in forward ground speed, coupled with a recovered updraft and tornadic vortex, allowed the tornado to continue for an additional 12 min, a time marked by consistent EF3 and common EF4 damage. This process, referred to as a failed occlusion, is thought to have been a result of a hybrid cyclic RFD process not yet seen in the literature. This hypothesis does not take into account thermodynamic data (which are not available for the storm in question), but serves as one possible explanation for the observations.

A number of different areas for future work exist with the data from this case. Comparisons with other area radars that were scanning volumetrically (e.g., the KTLX WSR-88D and the TOKC TDWR) could be used to piece together vortex tilt characteristics around the failed occlusion period. Polarimetric comparisons of the debris ejections and the characteristics of the southern surge at multiple frequencies can be made in order to relate the X-band PX-1000 observations with the S-band WSR-88D systems that are used operationally and in research modes (e.g., the KOUN WSR-88D). KOUN sector scans are available, which may allow for volumetric characterization of the debris contained in each RFGFS. Such comparisons would also be valuable to the development of the multilag concept, especially its occasional breakdown in areas of high spectrum width. These findings combined with comparisons with other datasets will make for increased accuracy in future low-power-pulse compression weather radar systems (Cheong et al. 2013b).

Additionally, despite the lack of extensive dual-Doppler coverage for the Moore tornado, numerical simulations of the failed occlusion processes from this case and future cases could prove instrumental in determining the validity and details of the proposed hypothesis. Polarimetric analysis of the statistical characteristics of debris and hydrometeors at all stages of the storm should be undertaken given the numerous polarimetric datasets from the case, specifically with regard to the apparent negative Z_{DR} mean in the TDS at early stages of the tornado. Finally, further investigation of the cell merger early in the tornado track is an intriguing area for future studies, and may aid in understanding its role in tornadogenesis in the Moore case.

Acknowledgments. This work was supported by the National Science Foundation under Grant AGS1303685. The authors thank Matthew Kumjian and two anonymous reviewers for thoughtful critiques of the paper that led to a substantially improved final product. The authors would also like to thank Don Burgess and Jeff Snyder for their detailed reviews of early versions of

the manuscript. Greg Stumpf, Rick Smith, and Gabe Garfield provided valuable discussions regarding the NWS damage survey of the 20 May Moore tornado. Alan Shapiro provided assistance with the dual-Doppler formulations. Jana Houser and Tim Bonin offered useful discussion and critique in various aspects of the study.

REFERENCES

Adlerman, E. J., and K. K. Droegemeier, 2005: The dependence of numerically simulated cyclic mesocyclogenesis upon environmental vertical wind shear. *Mon. Wea. Rev.,* **133,** 3595–3623, doi:10.1175/MWR3039.1.

——, ——, and R. Davies-Jones, 1999: A numerical simulation of cyclic mesocyclogenesis. *J. Atmos. Sci.,* **56,** 2045–2069, doi:10.1175/1520-0469(1999)056<2045:ANSOCM>2.0.CO;2.

Atkins, N. T., K. M. Butler, K. R. Flynn, and R. M. Wakimoto, 2014a: An integrated damage, visual, and radar analysis of the 2013 Moore Oklahoma EF5 tornado. *Bull. Amer. Meteor. Soc.,* **95,** 1549–1561, doi:10.1175/BAMS-D-14-00033.1.

——, E. M. Glidden, and T. M. Nicholson, 2014b: Observations of wall cloud formation in supercell thunderstorms during VORTEX2. *Mon. Wea. Rev.,* **142,** 4823–4838, doi:10.1175/MWR-D-14-00125.1.

Barnes, S. L., 1964: A technique for maximizing details in numerical weather map analysis. *J. Appl. Meteor.,* **3,** 396–409, doi:10.1175/1520-0450(1964)003<0396:ATFMDI>2.0.CO;2.

Beck, J. R., J. L. Schroeder, and J. M. Wurman, 2006: High-resolution dual-Doppler analyses of the 29 May 2001 Kress, Texas, cyclic supercell. *Mon. Wea. Rev.,* **134,** 3125–3148, doi:10.1175/MWR3246.1.

Biggerstaff, M. I., and Coauthors, 2005: The Shared Mobile Atmospheric Research and Teaching Radar: A collaboration to enhance research and teaching. *Bull. Amer. Meteor. Soc.,* **86,** 1263–1274, doi:10.1175/BAMS-86-9-1263.

Bluestein, H. B., and M. L. Weisman, 2000: The interaction of numerically simulated supercells initiated along lines. *Mon. Wea. Rev.,* **128,** 3128–3149, doi:10.1175/1520-0493(2000)128<3128:TIONSS>2.0.CO;2.

——, C. C. Weiss, and A. L. Pazmany, 2004: The vertical structure of a tornado near Happy, Texas, on 5 May 2002: High-resolution, mobile, W-band, Doppler radar observations. *Mon. Wea. Rev.,* **132,** 2325–2337, doi:10.1175/1520-0493(2004)132<2325:TVSOAT>2.0.CO;2.

——, M. M. French, R. L. Tanamachi, S. Frasier, K. Hardwick, F. Junyent, and A. L. Pazmany, 2007a: Close-range observations of tornadoes in supercells made with a dual-polarization, X-band, mobile Doppler radar. *Mon. Wea. Rev.,* **135,** 1522–1543, doi:10.1175/MWR3349.1.

——, C. C. Weiss, M. M. French, E. M. Holthaus, R. L. Tanamachi, S. Frasier, and A. L. Pazmany, 2007b: The structure of tornadoes near Attica, Kansas, on 12 May 2004: High-resolution, mobile, Doppler radar observations. *Mon. Wea. Rev.,* **135,** 475–506, doi:10.1175/MWR3295.1.

——, M. M. French, I. PopStefanija, R. T. Bluth, and J. B. Knorr, 2010: A mobile, phased-array Doppler radar for the study of severe convective storms. *Bull. Amer. Meteor. Soc.,* **91,** 579–600, doi:10.1175/2009BAMS2914.1.

Bodine, D. J., M. R. Kumjian, R. D. Palmer, P. L. Heinselman, and A. V. Ryzhkov, 2013: Tornado damage estimation using polarimetric radar. *Wea. Forecasting,* **28,** 139–158, doi:10.1175/WAF-D-11-00158.1.

——, R. D. Palmer, and G. Zhang, 2014: Dual-wavelength polarimetric radar analyses of tornadic debris signatures. *J. Appl. Meteor. Climatol.,* **53,** 242–261, doi:10.1175/JAMC-D-13-0189.1.

Brandes, E. A., 1978: Mesocyclone evolution and tornadogenesis: Some observations. *Mon. Wea. Rev.,* **106,** 995–1011, doi:10.1175/1520-0493(1978)106<0995:MEATSO>2.0.CO;2.

Bringi, V. N., V. Chandrasekar, N. Balakrishnan, and D. S. Zrnić, 1990: An examination of propagation effects in rainfall on radar measurements at microwave frequencies. *J. Atmos. Oceanic Technol.,* **7,** 829–840, doi:10.1175/1520-0426(1990)007<0829:AEOPEI>2.0.CO;2.

Brown, R. A., L. R. Lemon, and D. W. Burgess, 1978: Tornado detection by pulsed Doppler radar. *Mon. Wea. Rev.,* **106,** 29–38, doi:10.1175/1520-0493(1978)106<0029:TDBPDR>2.0.CO;2.

——, V. T. Wood, R. M. Steadham, R. R. Lee, B. A. Flickinger, and D. Sirmans, 2005: New WSR-88D volume coverage pattern 12: Results of field tests. *Wea. Forecasting,* **20,** 385–393, doi:10.1175/WAF848.1.

Burgess, D. W., V. T. Wood, and R. A. Brown, 1982: Mesocyclone evolution statistics. Preprints, *12th Conf. on Severe Local Storms,* San Antonio, TX, Amer. Meteor. Soc., 422–424.

——, and Coauthors, 2014: 20 May 2013 Moore, Oklahoma, tornado: Damage survey and analysis. *Wea. Forecasting,* **29,** 1229–1237, doi:10.1175/WAF-D-14-00039.1.

Cheong, B. L., R. Kelley, R. D. Palmer, Y. Zhang, M. Yeary, and T.-Y. Yu, 2013a: PX-1000: A solid-state polarimetric X-band weather radar and time-frequency multiplexed waveform for blind range mitigation. *IEEE Trans. Instrum. Measure.,* **62,** 3064–3072, doi:10.1109/TIM.2013.2270046.

——, J. M. Kurdzo, G. Zhang, and R. D. Palmer, 2013b: The impacts of multi-lag moment processor on a solid-state polarimetric weather radar. *36th Conf. on Radar Meteorology,* Breckenridge, CO, Amer. Meteor. Soc., 2B.2. [Available online at https://ams.confex.com/ams/36Radar/webprogram/Paper228464.html.]

Crowe, C. C., W. A. Petersen, L. D. Carey, and D. J. Cecil, 2010: A dual-polarization investigation of tornado-warned cells associated with Hurricane Rita (2005). *Electron. J. Oper. Meteor.,* **2010-EJ4,** 25 pp. [Available online at http://www.nwas.org/ej/pdf/2010-EJ4.pdf.]

Darkow, G. L., and J. C. Roos, 1970: Multiple tornado producing thunderstorms and their apparent cyclic variations in intensity. Preprints, *14th Conf. on Radar Meteorology,* Tucson, AZ, Amer. Meteor. Soc., 305–308.

Dawson, D. T., E. R. Mansell, Y. Jung, L. J. Wicker, M. R. Kumjian, and M. Xue, 2014: Low-level ZDR signatures in supercell forward flanks: The role of size sorting and melting of hail. *J. Atmos. Sci.,* **71,** 276–299, doi:10.1175/JAS-D-13-0118.1.

Dolan, B., and S. A. Rutledge, 2009: A theory-based hydrometeor identification algorithm for X-band polarimetric radars. *J. Atmos. Oceanic Technol.,* **26,** 2071–2088, doi:10.1175/2009JTECHA1208.1.

Doviak, R. J., and D. S. Zrnić, 1993: *Doppler Radar and Weather Observations.* Dover, 562 pp.

Dowell, D. C., and H. B. Bluestein, 2002a: The 8 June 1995 McLean, Texas, storm. Part I: Observations of cyclic tornadogenesis. *Mon. Wea. Rev.,* **130,** 2626–2648, doi:10.1175/1520-0493(2002)130<2626:TJMTSP>2.0.CO;2.

——, and ——, 2002b: The 8 June 1995 McLean, Texas, storm. Part II: Cyclic tornado formation, maintenance, and dissipation. *Mon. Wea. Rev.,* **130,** 2649–2670, doi:10.1175/1520-0493(2002)130<2649:TJMTSP>2.0.CO;2.

Finley, C. A., and B. D. Lee, 2004: High resolution mobile mesonet observations of RFD surges in the June 9 Basset, Nebraska supercell during Project ANSWERS 2003. Preprints, *22nd Conf. on Severe Local Storms,* Hyannis, MA, Amer. Meteor. Soc., P11.3. [Available online at https://ams.confex.com/ams/11aram22sls/techprogram/paper_82005.htm.]

——, and ——, 2008: Mobile mesonet observations of an intense RFD and multiple RFD gust fronts in the May 23 Quinter, Kansas tornadic supercell during TWISTEX 2008. Preprints, *24th Conf. on Severe Local Storms,* Savannah, GA, Amer. Meteor. Soc., P3.18. [Available online at https://ams.confex.com/ams/24SLS/techprogram/paper_142133.htm.]

French, M. M., H. B. Bluestein, D. C. Dowell, L. J. Wicker, M. R. Kramar, and A. L. Pazmany, 2008: High-resolution, mobile Doppler radar observations of cyclic mesocyclogenesis in a supercell. *Mon. Wea. Rev.,* **136,** 4997–5016, doi:10.1175/2008MWR2407.1.

——, ——, I. PopStefanija, C. A. Baldi, and R. T. Bluth, 2013: Reexamining the vertical development of tornadic vortex signatures in supercells. *Mon. Wea. Rev.,* **141,** 4576–4601, doi:10.1175/MWR-D-12-00315.1.

——, ——, ——, ——, and ——, 2014: Mobile, phased-array, Doppler radar observations of tornadoes at X band. *Mon. Wea. Rev.,* **142,** 1010–1036, doi:10.1175/MWR-D-13-00101.1.

——, D. W. Burgess, E. R. Mansell, and L. J. Wicker, 2015: Bulk hook echo raindrop sizes retrieved using mobile, polarimetric Doppler radar observations. *J. Appl. Meteor. Climatol.,* **54,** 423–450, doi:10.1175/JAMC-D-14-0171.1.

Fujita, T. T., D. L. Bradbury, and C. F. van Thullenar, 1970: Palm Sunday tornadoes of April 11, 1965. *Mon. Wea. Rev.,* **98,** 29–69, doi:10.1175/1520-0493(1970)098<0029:PSTOA>2.3.CO;2.

Grzych, M. L., B. D. Lee, and C. A. Finley, 2007: Thermodynamic analysis of supercell rear-flank downdrafts from Project ANSWERS. *Mon. Wea. Rev.,* **135,** 240–246, doi:10.1175/MWR3288.1.

Hastings, R. M., Y. P. Richardson, and P. M. Markowski, 2014: Simulation of near-surface mesocyclogenesis during mergers between mature and nascent supercells. *27th Conf. on Severe Local Storms,* Madison, WI, Amer. Meteor. Soc., 3B.2. [Available online at https://ams.confex.com/ams/27SLS/webprogram/Paper255837.html.]

Heinselman, P. L., and S. M. Torres, 2011: High-temporal-resolution capabilities of the national weather radar testbed phased-array radar. *J. Appl. Meteor. Climatol.,* **50,** 579–593, doi:10.1175/2010JAMC2588.1.

——, D. L. Priegnitz, K. L. Manross, T. M. Smith, and R. W. Adams, 2008: Rapid sampling of severe storms by the national weather radar testbed phased array radar. *Wea. Forecasting,* **23,** 808–824, doi:10.1175/2008WAF2007071.1.

Herzegh, P. H., and A. R. Jameson, 1992: Observing precipitation through dual-polarization radar measurements. *Bull. Amer. Meteor. Soc.,* **73,** 1365–1374, doi:10.1175/1520-0477(1992)073<1365:OPTDPR>2.0.CO;2.

Hirth, B. D., J. L. Schroeder, and C. C. Weiss, 2008: Surface analysis of the rear-flank downdraft outflow in two tornadic supercells. *Mon. Wea. Rev.,* **136,** 2344–2363, doi:10.1175/2007MWR2285.1.

Houser, J. B., 2013: Observations of supercell tornado evolution using a mobile, rapid-scan, X-band radar. Ph.D. thesis, University of Oklahoma, 264 pp.

——, H. B. Bluestein, and J. C. Snyder, 2015: Rapid-scan, polarimetric, Doppler radar observations of tornadogenesis and tornado dissipation in a tornadic supercell: The "El Reno, Oklahoma" storm of 24 May 2011. *Mon. Wea. Rev.,* in press.

Isom, B., and Coauthors, 2013: The atmospheric imaging radar: Simultaneous volumetric observations using a phased array weather radar. *J. Atmos. Oceanic Technol.,* **30,** 655–675, doi:10.1175/JTECH-D-12-00063.1.

Jameson, A. R., 1992: The effect of temperature on attenuation-correction schemes in rain using polarization propagation differential phase shift. *J. Appl. Meteor.,* **31,** 1106–1118, doi:10.1175/1520-0450(1992)031<1106:TEOTOA>2.0.CO;2.

Klemp, J. B., and R. Rotunno, 1983: A study of the tornadic region within a supercell thunderstorm. *J. Atmos. Sci.,* **40,** 359–377, doi:10.1175/1520-0469(1983)040<0359:ASOTTR>2.0.CO;2.

Kosiba, K., and J. Wurman, 2010: The three-dimensional axisymmetric wind field structure of the Spencer, South Dakota, 1998 tornado. *J. Atmos. Sci.,* **67,** 3074–3083, doi:10.1175/2010JAS3416.1.

——, and ——, 2013: The three-dimensional structure and evolution of a tornado boundary layer. *Wea. Forecasting,* **28,** 1552–1561, doi:10.1175/WAF-D-13-00070.1.

——, ——, Y. Richardson, P. Markowski, P. Robinson, and J. Marquis, 2013: Genesis of the Goshen County, Wyoming, tornado on 5 June 2009 during VORTEX2. *Mon. Wea. Rev.,* **141,** 1157–1181, doi:10.1175/MWR-D-12-00056.1.

Kumjian, M. R., 2011: Precipitation properties of supercell hook echoes. *Electron. J. Severe Storms Meteor.,* **6** (5). [Available online at http://ejssm.org/ojs/index.php/ejssm/article/viewArticle/93.]

——, and A. V. Ryzhkov, 2008: Polarimetric signatures in supercell thunderstorms. *J. Appl. Meteor. Climatol.,* **47,** 1940–1961, doi:10.1175/2007JAMC1874.1.

——, and ——, 2009: Storm-relative helicity revealed from polarimetric radar measurements. *J. Atmos. Sci.,* **66,** 667–685, doi:10.1175/2008JAS2815.1.

——, ——, V. M. Melnikov, and T. J. Schuur, 2010: Rapid-scan super-resolution observations of a cyclic supercell with a dual-polarization WSR-88D. *Mon. Wea. Rev.,* **138,** 3762–3786, doi:10.1175/2010MWR3322.1.

Kurdzo, J. M., B. L. Cheong, R. D. Palmer, G. Zhang, and J. Meier, 2014: A pulse compression waveform for improved-sensitivity weather radar observations. *J. Atmos. Oceanic Technol.,* **31,** 2713–2731, doi:10.1175/JTECH-D-13-00021.1.

Lee, B. D., B. F. Jewett, and R. B. Wilhelmson, 2006: The 19 April 1996 Illinois tornado outbreak. Part II: Cell mergers and associated tornado incidence. *Wea. Forecasting,* **21,** 449–464, doi:10.1175/WAF943.1.

——, C. A. Finley, and C. D. Karstens, 2012: The Bowdle, South Dakota, cyclic tornadic supercell of 22 May 2010: Surface analysis of rear-flank downdraft evolution and multiple internal surges. *Mon. Wea. Rev.,* **140,** 3419–3441, doi:10.1175/MWR-D-11-00351.1.

Lee, E. T. Y., 1989: Choosing nodes in parametric curve interpolation. *Comput. Aided Des.,* **21,** 363–370, doi:10.1016/0010-4485(89)90003-1.

Lei, L., G. Zhang, R. J. Doviak, R. Palmer, B. L. Cheong, M. Xue, Q. Cao, and Y. Li, 2012: Multilag correlation estimators for polarimetric radar measurements in the presence of noise. *J. Atmos. Oceanic Technol.,* **29,** 772–795, doi:10.1175/JTECH-D-11-00010.1.

Lemon, L. R., and C. A. Doswell, 1979: Severe thunderstorm evolution and mesocyclone structure as related to tornadogenesis. *Mon. Wea. Rev.,* **107,** 1184–1197, doi:10.1175/1520-0493(1979)107<1184:STEAMS>2.0.CO;2.

Magsig, M. A., and J. T. Snow, 1998: Long-distance debris transport by tornadic thunderstorms. Part I: The 7 May 1995 supercell thunderstorm. *Mon. Wea. Rev.,* **126,** 1430–1449, doi:10.1175/1520-0493(1998)126<1430:LDDTBT>2.0.CO;2.

Majcen, M., P. Markowski, Y. Richardson, D. Dowell, and J. Wurman, 2008: Multipass objective analyses of Doppler radar data. *J. Atmos. Oceanic Technol.,* **25,** 1845–1858, doi:10.1175/2008JTECHA1089.1.

Markowski, P. M., 2002: Hook echoes and rear-flank downdrafts: A review. *Mon. Wea. Rev.,* **130,** 852–876, doi:10.1175/1520-0493(2002)130<0852:HEARFD>2.0.CO;2.

——, and Coauthors, 2012: The pretornadic phase of the Goshen County, Wyoming, supercell of 5 June 2009 intercepted by VORTEX2. Part I: Evolution of kinematic and surface thermodynamic fields. *Mon. Wea. Rev.,* **140,** 2887–2915, doi:10.1175/MWR-D-11-00336.1.

——, J. M. Straka, and E. N. Rasmussen, 2002: Direct surface thermodynamic observations within the rear-flank downdrafts of nontornadic and tornadic supercells. *Mon. Wea. Rev.,* **130,** 1692–1721, doi:10.1175/1520-0493(2002)130<1692:DSTOWT>2.0.CO;2.

Marquis, J., Y. Richardson, J. Wurman, and P. Markowski, 2008: Single- and dual-Doppler analysis of a tornadic vortex and surrounding storm-scale flow in the Crowell, Texas, supercell of 30 April 2000. *Mon. Wea. Rev.,* **136,** 5017–5043, doi:10.1175/2008MWR2442.1.

——, ——, P. Markowski, D. Dowell, and J. Wurman, 2012: Tornado maintenance investigated with high-resolution dual-Doppler and EnKF analysis. *Mon. Wea. Rev.,* **140,** 3–27, doi:10.1175/MWR-D-11-00025.1.

Palmer, R. D., and Coauthors, 2011: Observations of the 10 May 2010 tornado outbreak using OU-PRIME: Potential for new science with high-resolution polarimetric radar. *Bull. Amer. Meteor. Soc.,* **92,** 871–891, doi:10.1175/2011BAMS3125.1.

Park, S. G., V. N. Bringi, V. Chandrasekar, M. Maki, and K. Iwanami, 2005: Correction of radar reflectivity and differential reflectivity for rain attenuation at X band. Part I: Theoretical and empirical basis. *J. Atmos. Oceanic Technol.,* **22,** 1621–1632, doi:10.1175/JTECH1803.1.

Pazmany, A. L., J. B. Mead, H. B. Bluestein, J. C. Snyder, and J. B. Houser, 2013: A mobile rapid-scanning X-band polarimetric (RaXPol) Doppler radar system. *J. Atmos. Oceanic Technol.,* **30,** 1398–1413, doi:10.1175/JTECH-D-12-00166.1.

Ryzhkov, A. V., and D. S. Zrnić, 1995: Comparison of dual-polarization radar estimators of rain. *J. Atmos. Oceanic Technol.,* **12,** 249–256, doi:10.1175/1520-0426(1995)012<0249:CODPRE>2.0.CO;2.

——, D. Burgess, D. Zrnić, T. Smith, and S. Giangrande, 2002: Polarimetric analysis of a 3 May 1999 tornado. Preprints, *21st Conf. on Severe Local Storms,* San Antonio, TX, Amer. Meteor. Soc., 14.2. [Available online at https://ams.confex.com/ams/SLS_WAF_NWP/techprogram/paper_47348.htm.]

——, T. J. Schurr, D. W. Burgess, and D. Zrnić, 2005: Polarimetric tornado detection. *J. Appl. Meteor.,* **44,** 557–570, doi:10.1175/JAM2235.1.

Schultz, C. J., and Coauthors, 2012: Dual-polarization tornadic debris signatures. Part I: Examples and utility in an operational setting. *Electron. J. Operat. Meteor.,* **13** (9), 120–137. [Available online at http://www.nwas.org/ej/pdf/2012-EJ9.pdf.]

Shapiro, A., and J. J. Mewes, 1999: New formulations of dual-Doppler wind analysis. *J. Atmos. Oceanic Technol.,* **16,** 782–792, doi:10.1175/1520-0426(1999)016<0782:NFODDW>2.0.CO;2.

Skinner, P. S., C. C. Weiss, M. M. French, H. B. Bluestein, P. M. Markowski, and Y. P. Richardson, 2014: VORTEX2 observations of a low-level mesocyclone with multiple internal rear-flank downdraft momentum surges in the 18 May 2010, Dumas, Texas supercell. *Mon. Wea. Rev.,* **142,** 2935–2960, doi:10.1175/MWR-D-13-00240.1.

Snyder, J. C., and H. B. Bluestein, 2014: Some considerations for the use of high-resolution mobile radar data in tornado intensity determination. *Wea. Forecasting,* **29,** 799–827, doi:10.1175/WAF-D-14-00026.1.

——, and A. V. Ryzhkov, 2014: An automated detection for polarimetric tornado debris detection. *Eighth European Conf. on Radar in Meteorology and Hydrology,* Garmisch-Partenkirchen, Germany, Deutscher Wetterdienst, MES.P21.

——, H. B. Bluestein, G. Zhang, and S. J. Frasier, 2010: Attenuation correction and hydrometeor classification of high-resolution, X-band, dual-polarized mobile radar measurements in severe convective storms. *J. Atmos. Oceanic Technol.,* **27,** 1979–2001, doi:10.1175/2010JTECHA1356.1.

——, ——, V. Venkatesh, and S. J. Frasier, 2013: Observations of polarimetric signatures in supercells by an X-band mobile Doppler radar. *Mon. Wea. Rev.,* **141,** 3–29, doi:10.1175/MWR-D-12-00068.1.

Tanamachi, R. L., H. B. Bluestein, J. B. Houser, S. J. Frasier, and K. M. Hardwick, 2012: Mobile, X-band, polarimetric Doppler radar observations of the 4 May 2007 Greensburg, Kansas, tornadic supercell. *Mon. Wea. Rev.,* **140,** 2103–2125, doi:10.1175/MWR-D-11-00142.1.

Weiss, C. C., 2009: The TTUKa mobile Doppler radar: Coordinated radar and in situ measurements of supercell thunderstorms during Project VORTEX2. *34th Conf. on Radar Meteorology,* Williamsburg, VA, Amer. Meteor. Soc., 11B.2. [Available online at https://ams.confex.com/ams/34Radar/techprogram/paper_155425.htm.]

Wicker, L. J., and R. B. Wilhelmson, 1995: Simulation and analysis of tornado development and decay within a three-dimensional supercell thunderstorm. *J. Atmos. Sci.,* **52,** 2675–2703, doi:10.1175/1520-0469(1995)052<2675:SAAOTD>2.0.CO;2.

Wurman, J., and M. Randall, 2001: An inexpensive, mobile, rapid-scan radar. Preprints, *30th Int. Conf. on Radar Meteorology,* Munich, Germany, Amer. Meteor. Soc., P3.4. [Available online at https://ams.confex.com/ams/30radar/techprogram/paper_21577.htm.]

——, and C. R. Alexander, 2005: The 30 May 1998 Spencer, South Dakota, storm. Part II: Comparison of observed damage and radar-derived winds in the tornadoes. *Mon. Wea. Rev.,* **133,** 97–119, doi:10.1175/MWR-2856.1.

——, and K. Kosiba, 2013: Finescale radar observations of tornado and mesocyclone structures. *Wea. Forecasting,* **28,** 1157–1174, doi:10.1175/WAF-D-12-00127.1.

——, Y. Richardson, C. Alexander, S. Weygandt, and P. F. Zhang, 2007: Dual-Doppler and single-Doppler analysis of a tornadic storm undergoing mergers and repeated tornadogenesis. *Mon. Wea. Rev.,* **135,** 736–758, doi:10.1175/MWR3276.1.

——, K. Kosiba, P. Markowski, Y. Richardson, D. Dowell, and P. Robinson, 2010: Finescale single- and dual-Doppler analysis of tornado intensification, maintenance, and dissipation in the Orleans, Nebraska, supercell. *Mon. Wea. Rev.,* **138,** 4439–4455, doi:10.1175/2010MWR3330.1.

——, D. Dowell, Y. Richardson, P. Markowski, E. Rasmussen, D. Burgess, L. Wicker, and H. B. Bluestein, 2012: The second verification of the origins of rotation in tornadoes experiment: VORTEX2. *Bull. Amer. Meteor. Soc.,* **93,** 1147–1170, doi:10.1175/BAMS-D-11-00010.1.

Ziegler, C. L., E. N. Rasmussen, T. R. Shepherd, A. I. Watson, and J. M. Straka, 2001: The evolution of low-level rotation in the 29 May 1994 Newcastle–Graham, Texas, storm complex during VORTEX. *Mon. Wea. Rev.,* **129,** 1339–1368, doi:10.1175/1520-0493(2001)129<1339:TEOLLR>2.0.CO;2.